

3.4 DST Heating Schedule -- Workshop Discussions

Discussions were held during the June 8, 2001 workshop regarding the scheduled heater shut-off for the Drift Scale Test. The test will surpass four years of heating after December 3, 2001. Workshop participants agreed that power to the canister and wing heaters are shut-off at the end of four years, indicating the start of a cooling phase. Results from recent thermal calculations were presented that predict heated drift wall temperatures of about 80 degrees C after 3 years of cooling. These predicted temperatures are discussed in detail in the following section.

Principal Investigators representing each of the coupled process models presented their ideas and opinions regarding heater shut-off. No one advocated extending the heating phase beyond the original 4-year plan. The thermal-chemical process group requested 1 or 2 new core holes for investigating the geochemical properties of the rock in and around the boiling zone at the time of shut-off. Core from these holes will undergo an ultracentrifuge water extraction process with support from the USGS. The thermal-hydrologic process group recommended extending the date of heater shut-off by a month because more frequent monitoring of moisture movement through the rock, immediately upon cooling, wouldn't be hampered by holiday shutdown of the ESF. The thermal-mechanical group was interested in installing 5 tiltmeters in holes surrounding the heated drift. Tiltmeters would monitor expected movement in the rock following heater shut-off. This group also requested more frequent observations of the heated drift crown to look for cracking or greater volume of loose rock held in the welded wire mesh. These observations would be made from the viewing window at the bulkhead or from images recorded with the remote camera.

3.5 Predictive Simulations of the Cooling Phase in the Drift Scale Test

The heating cycle in the Drift Scale Test (DST), which is expected to continue for four years, is scheduled to end on December 3, 2001. It is therefore expedient at this time to perform predictive simulations about the cooling phase of the DST. These predictive simulations delineate the spatial and temporal evolution of the thermal-hydrological (TH) processes during the cooling phase and help to determine what useful data can be collected during the same. The results from these predictive simulations were presented during the 12th Thermal Test Workshop at Las Vegas, Nevada, on June 7th and 8th, 2001.

Predictive simulations for the cooling phase of the DST are based on the same conceptual model as has been used for simulating the heating phase. This model uses the integral finite-difference TOUGH2 simulator along with a dual-permeability conceptualization of the interactions between the rock matrix blocks and the fractures embedded in them. The wing heaters in this model are incorporated as high-permeability conduits. At the time of performing the predictive simulations for the cooling phase, the DST was at 39 months of heating. Since the cooling phase is to begin only after 48 months of heating, the heating phase was allowed to continue till 48 months with the heating power available at the end of the 39 months (March 2001) of heating.

These predictive simulations are expected to provide us with guidelines for scheduling the active testing during the cooling phase of the DST. One important issue during this phase is to find out the rate at which the rock cools once the heaters are switched off. Another important TH issue that needs to be considered is the duration of the two-phase zone (evidenced by 'heat-pipe signatures) during cooling. This will provide evidence of TH coupling. These predictive simulations are also to demonstrate the expected changes in moisture redistribution both in the fractures and in the matrix rock blocks. While the changes in fracture liquid saturation will guide the scheduling of air-permeability testing, the changes in matrix liquid saturation will govern the frequency of geophysical measurements.

To determine the rate at which the rock will cool off in the DST following heater switch-off, we first show the simulated contours of temperatures at four years of heating in the plane of hydrology boreholes 57-61 (see Figure 24). Observe that borehole 60, in comparison to the other boreholes in this group, is intersected by the maximum number of temperature contours, in other words, the temperature gradient is steepest along borehole 60. Therefore the sensors in this borehole are likely to register maximum changes in temperature during cooling. Thus, a study of the simulated temperatures in borehole 60 may give us an indication of how fast the rock is going to lose heat. In addition, we will investigate the temperature history in RTD borehole 160 and at the drift wall. Borehole 160 is a horizontal hole running parallel to the wing heaters. Historically, this borehole and the drift wall, due to their proximity to the source of heat, have registered the maximum temperatures. These will therefore be good locations for monitoring the drops in temperature during the cooling phase.

In Figures 25a and 25b, we show the simulated temperature history at the drift surface during the cooling phase. Figure 25a shows the temperature at the drift surface as a

function of time during cooling, while Figure 25b shows the drop in temperature at the drift surface from its pre-cooling value at the drift surface. Temperature at the drift surface decreases rapidly during the initial phases of cooling, before reaching an asymptotic rate of decline. For example, after one year of cooling, the drift surface temperature has declined by 120°C, whereas the drop is only 140°C after two years of cooling. Note also that, after two years of cooling, the temperature at the drift surface is expected to be well below the nominal boiling point of water. Similar trends are observed in the simulated temperatures from borehole 160. Figures 26a and 26b are similar to Figures 25a and 25b, respectively, except that here the results are for selected sensors in borehole 160. Sensor 17 in borehole 160 was recording the maximum temperature during heating. This sensor exhibits the fastest rate of decline in temperature during cooling. After two years of cooling, all the sensors in borehole 160, including sensor 17, are expected to be below the nominal boiling point. The drop in temperature in various sensors of hydrology borehole 60 follows a similar pattern (see Figures 27a-b). In short, after two years of cooling, even the locations with maximum pre-cooling temperatures are predicted to decline below 100°C.

In addition, note that there is no evidence of heat-pipe signature as temperature approaches boiling during cooling in any of the selected boreholes. This is because, in contrast to the situation during heating, no vapor is produced during cooling. This implies that, except at the immediate onset of cooling, little movement of water in the fractures is expected during the cooling phase of the DST. To illustrate, contours of fracture liquid saturation at onset of cooling (Figure 28a) and at 3 months (Figure 28b), 6 months (Figure 28c) and 12 months (Figure 28d) since initiation of cooling are shown in Figures 28a-d. During the heating phase at the DST, there was a build-up of condensate outside the dry-out zone surrounding the Heated Drift and the wing heaters. At the initiation of cooling, this accumulated condensate drains through the fractures. Due to this rapid drainage at the start of cooling, liquid saturation in the fractures in the pre-cooling condensate zones decreases rapidly (within the first year or so). This has a direct impact on air-permeability testing. It is expected that, because of the decreasing liquid saturation in the fractures, air-injection testing will exhibit an increase in permeability during the first year since initiation of cooling. After that time, no appreciable increase in air-permeability values will be noticeable. However, these increases in air-permeability values are expected to be detected by testing in only the boreholes above the Heated Drift, as these boreholes will be located in the drying zone during the first year of cooling. The boreholes below the Heated Drift will not provide much information regarding increases in air-permeability values, as drying below the Heated Drift happens outside the range of these boreholes. Contours of liquid saturation in the matrix are shown in Figures 29a-d. While Figure 6a shows the matrix saturation at the beginning of cooling, Figure 29b, 29c, and 29d show the same at one year, two years and four years of cooling, respectively. As expected, liquid saturation in the matrix remains almost unchanged throughout the cooling phase at the DST. During cooling, rewetting of the dry-out zone, at the edge of the condensate zone, may happen through capillary suction. Since water movement in the fractures is very limited during cooling, such rewetting, a slow process in itself, of the rock matrix is expected to be very limited in nature. Since geophysical measurements are volume-averaged methods, such small, localized changes

in matrix saturation may be difficult to capture by these measurements. Thus, it is anticipated that geophysical measurements may not produce much new information during cooling. However, we recommend that geophysical surveys be carried out frequently during the first year since initiation of cooling. The frequency of survey can be reduced after that time period.

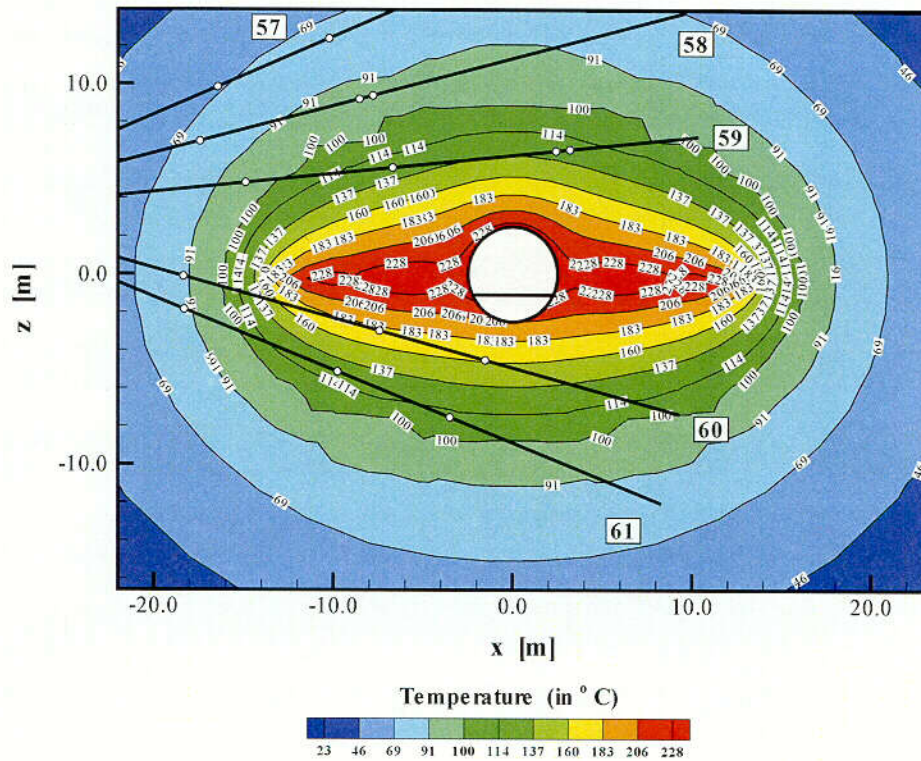
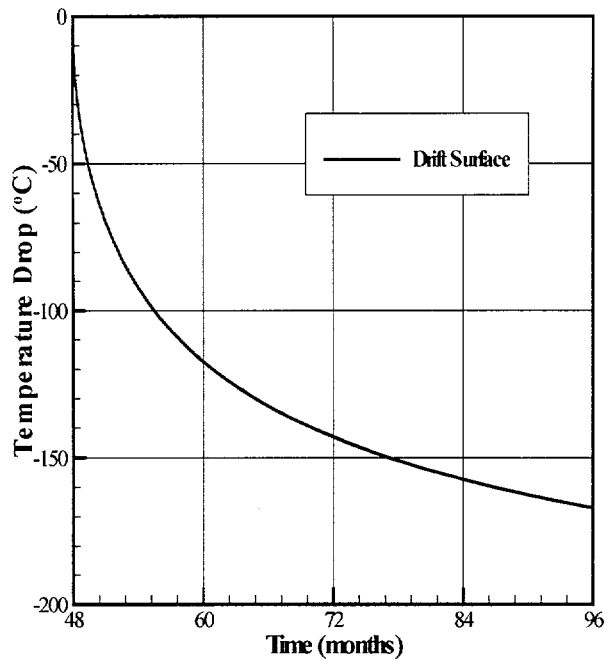
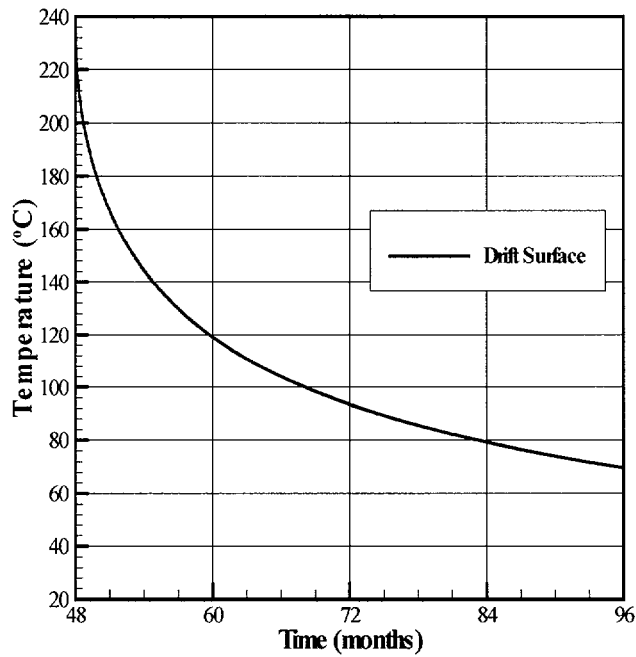


Figure 24. Contours of Simulated Temperature in the Plane of Hydrology Boreholes 57-61 at the End of 48 Months of Heating in the DST.



(a)



(b)

Figure 25. Simulated Temperature History at the Drift Wall During the Cooling Phase, (a) Temperature and (b) Drop in Temperature from Pre-Cooling Value.

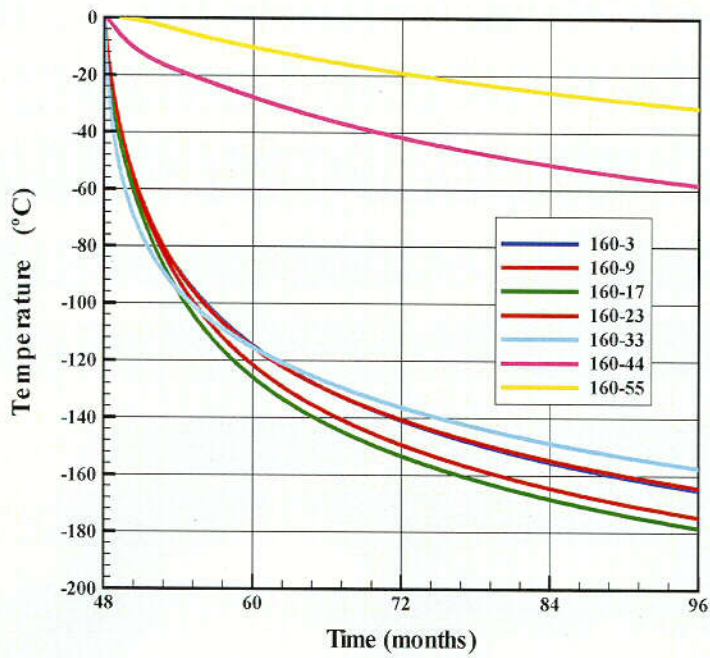
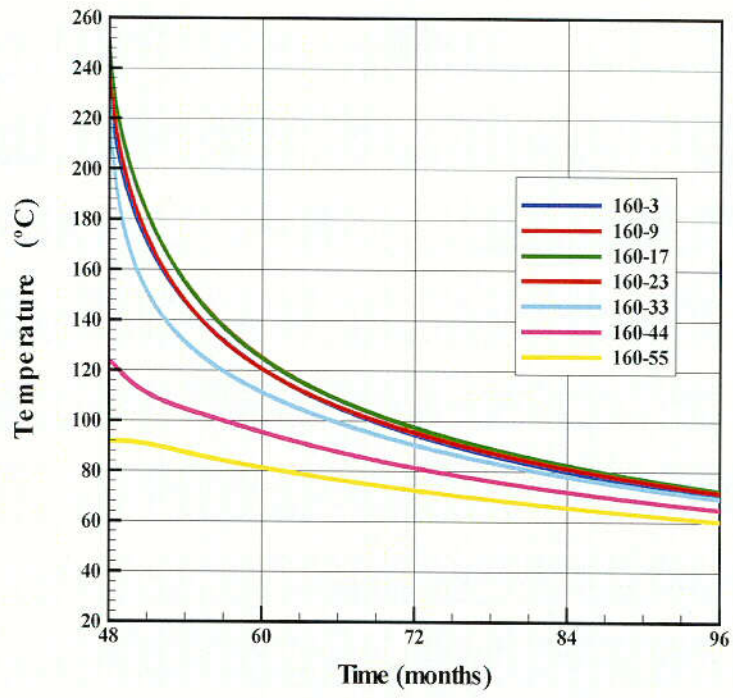


Figure 26. Simulated Temperature History at Selected Sensors of Borehole 160, (a) Temperature and (b) Drop in Temperature from Pre-Cooling Value.

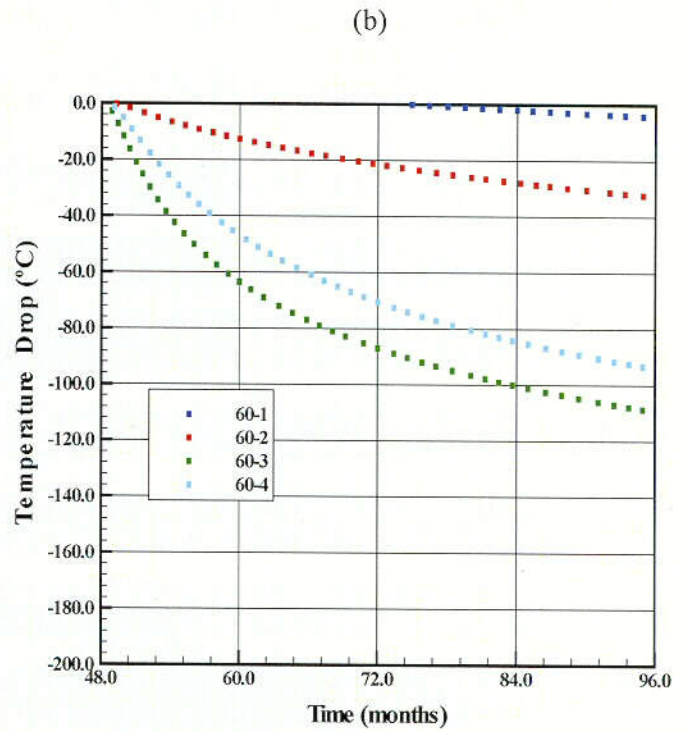
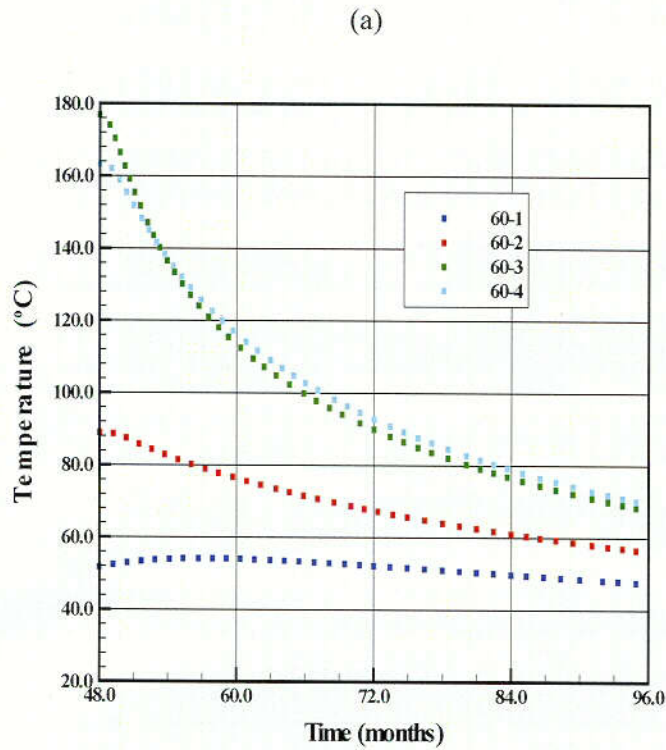


Figure 27. Simulate temperature history at all sensors of hydrology borehole 60, (a) Temperature and (b) Drop in temperature from its pre-cooling value.

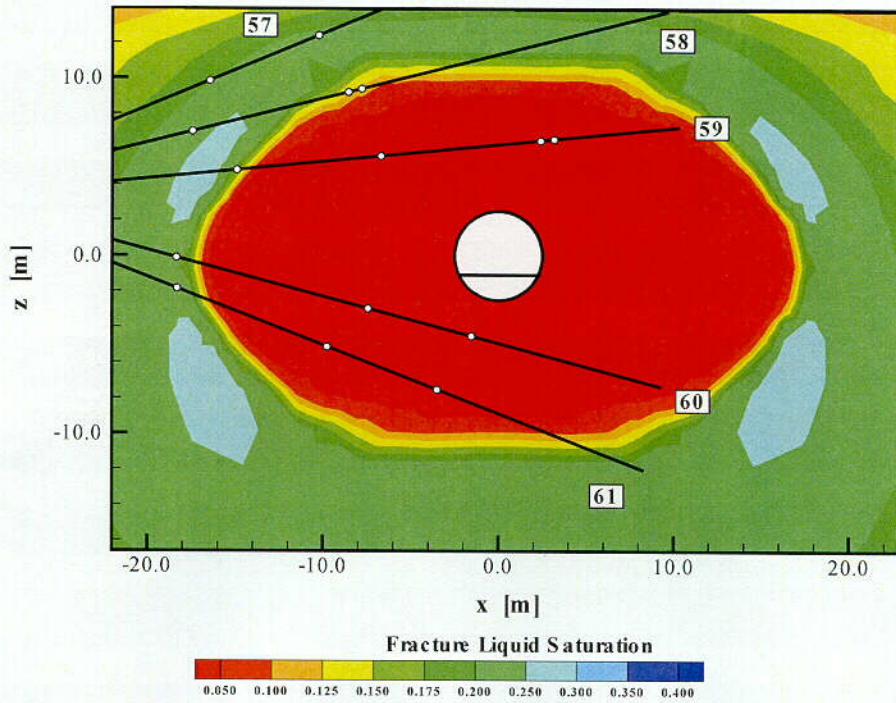
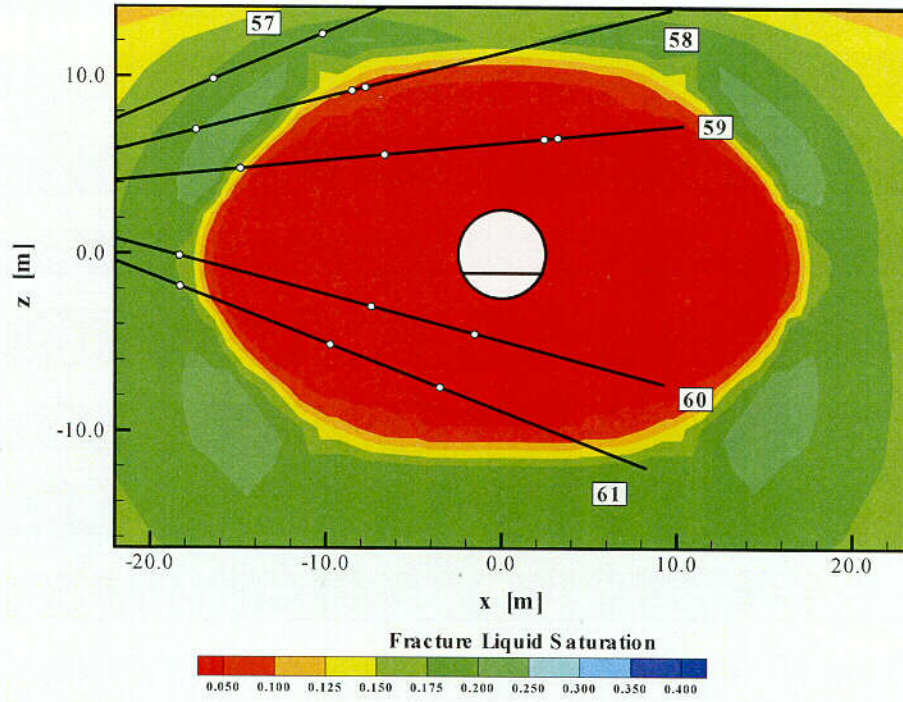


Figure 28. Simulated Contours of Liquid Saturation in the Fractures at (a) Beginning of Cooling, (b) 3 Months Since Beginning of Cooling.

C04

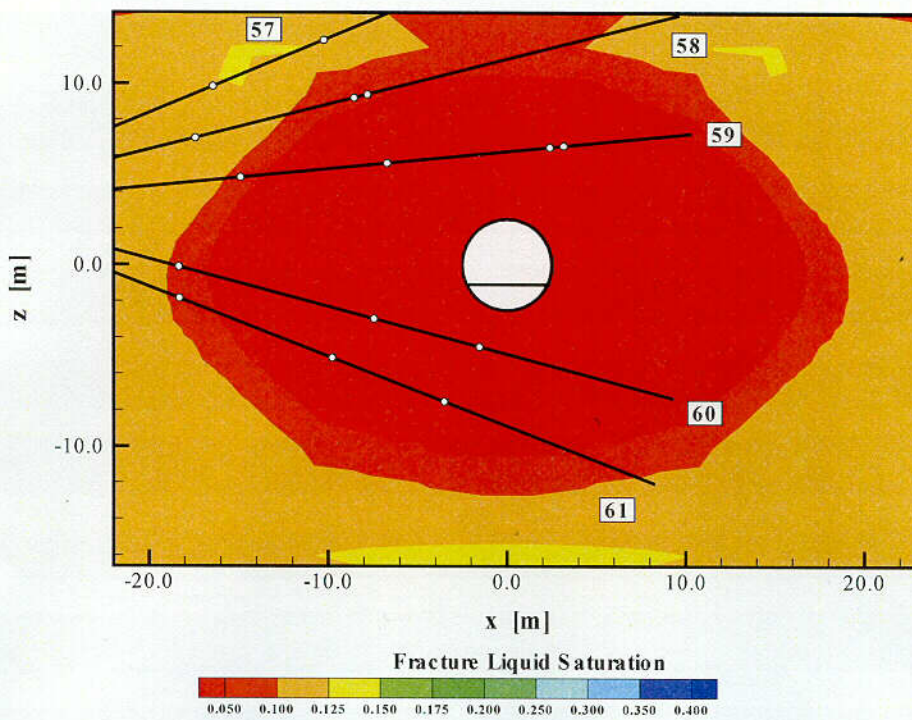
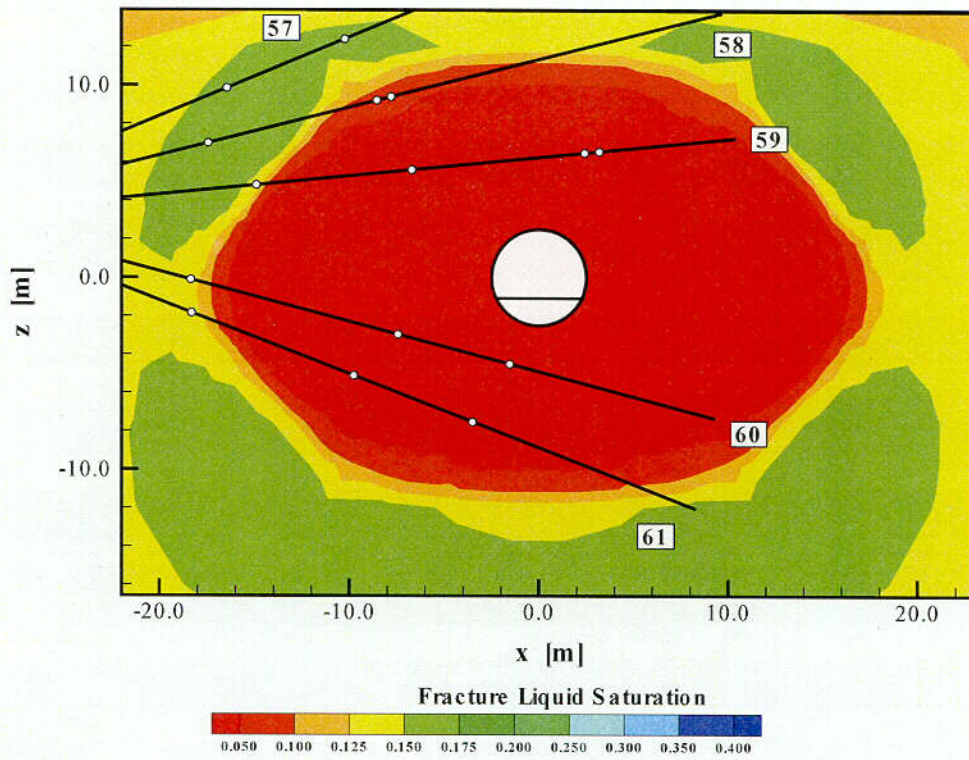


Figure 28. (Continued) Simulated Contours of Liquid Saturation in the Fractures at (c) 6 Months Since Beginning of Cooling and (d) 12 Months Since Beginning of Cooling.

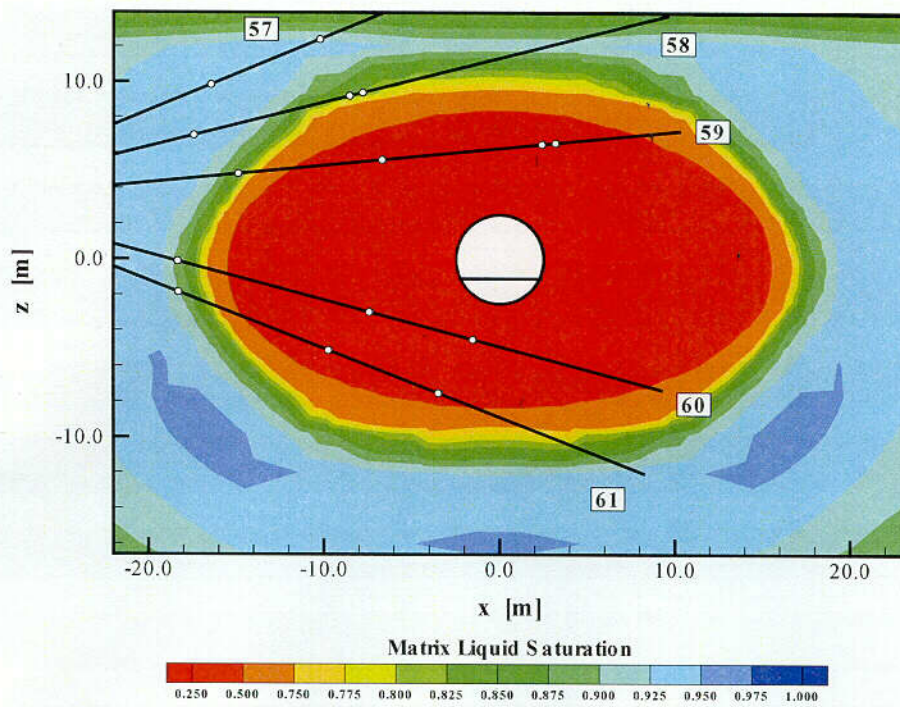
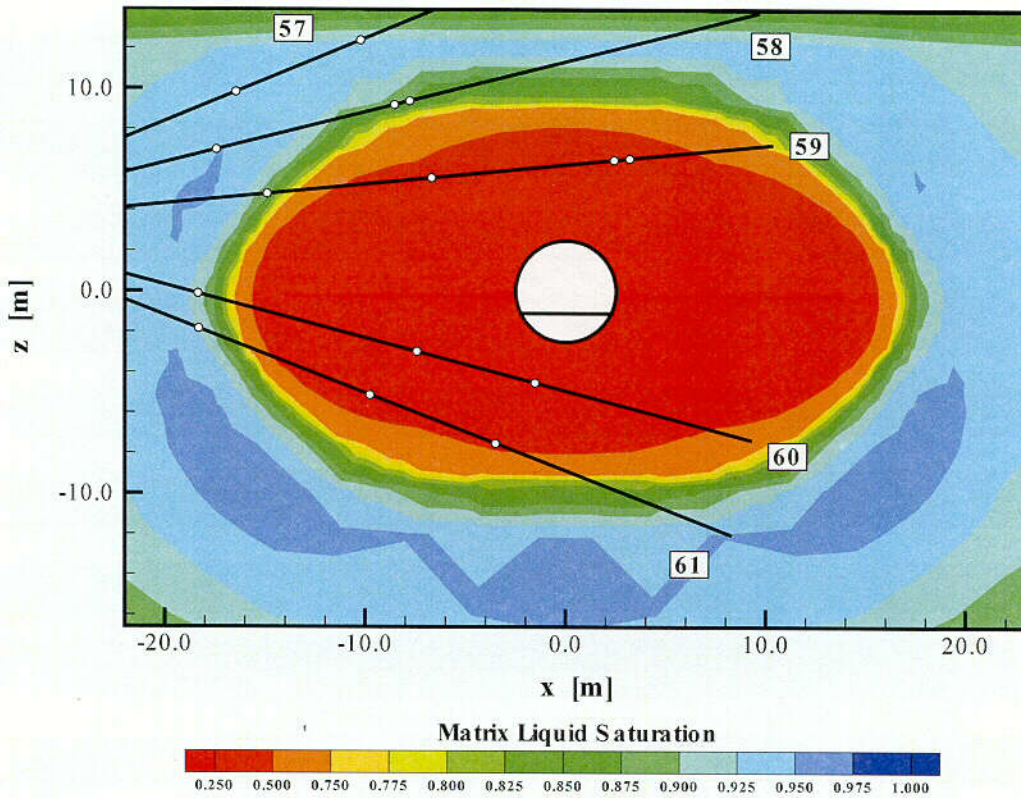


Figure 29. Simulated Contours of Liquid Saturation in the Matrix at (a) Beginning of Cooling, (b) One Year After Beginning of Cooling.

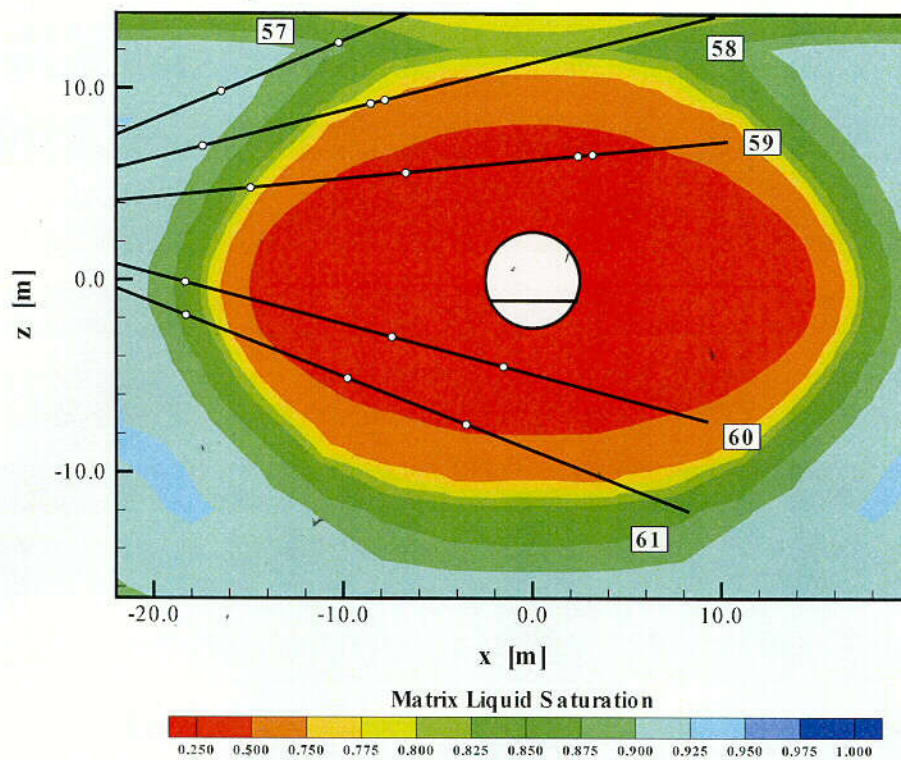
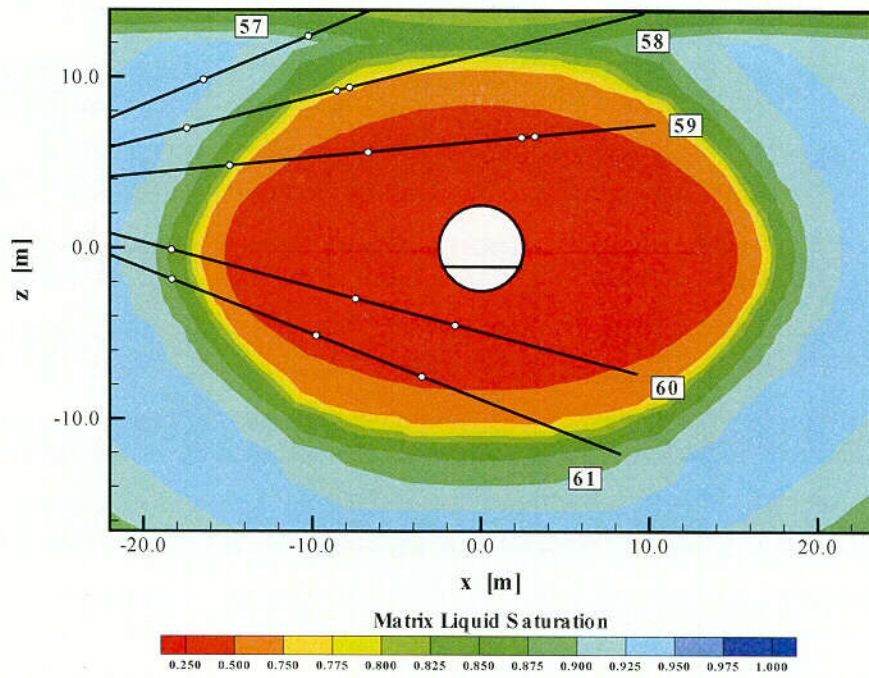


Figure 29. (Continued) Simulated Contours of Liquid Saturation in the Matrix at (c) Two Years After Beginning of Cooling and (d) Four Years After Beginning of Cooling.

INTENTIONALLY LEFT BLANK

4 Thermal-Hydrological Processes

Discussions of thermal-hydrological processes are included in the following four sections. Section 4.1 presents information regarding the field thermal tests. Section 4.2 presents the ground penetrating radar, Section 4.3 discusses thermal-hydrological model validation, and Section 4.4 examines data from borehole 79 in the context of temperature and fluid movement as impacted by neutron logging.

4.1 Field Thermal Tests - The Effect of Heat on the Movement of Water

The movement of water is one of the most important processes to be investigated in the site characterization of a potential nuclear waste repository at Yucca Mountain, Nevada. Understanding the process of the water movement under the influence of the radioactive decay heat of the nuclear waste will enhance the accuracy of predicting hydrological and chemical conditions in emplacement drifts and the transport of radioactive nuclides from the emplacement drifts to the accessible environment. The potential repository horizon in Yucca Mountain is a partially saturated Topopah Spring tuff formation, which is highly fractured, densely welded, with variable porosity of lithophysal cavity. The potential repository horizon will reside in both non-lithophysal and lithophysal units of the Topopah Spring tuff formation. It has been estimated that the pore space in the rock is about 90% saturated with pore water in the non-lithophysal unit, and about 70% saturated in the lithophysal unit.

The conceptual model of the effect of the heat on the movement of water is that the heat evaporates the pore water into vapor; the water vapor flows from the matrix into near-by fractures following pressure gradients. The vapor will take the least resistant paths by flowing in fractures. The water vapor will condense into liquid water in the fractures at the cooler regions. The condensate may be imbibed into the matrix or flows along fractures under the influence of gravity. Dependent on the combined effects of gravity and fracture orientation, the condensate may be shed away from the heat source or flows toward the heat source. The condensate that is shed away from the heat source will no longer be available for subsequent phase of the thermal-hydrological process. The condensate that is imbibed into the matrix will increase the water saturation level of the rock matrix, which will affect the TH process during the later period of the heating phase. The condensate that flows back toward the heat source may be evaporated/boiled again, and another cycle of vapor flow, condensation, and condensate flow will start again.

In the Drift Scale Test (DST), the heat-driven water movement is monitored by various means. The change of water saturation in the rock mass caused by the water movement is measured by geophysical methods, such as neutron logging, ground-penetrating radar (GPR), and electrical resistance tomography (ERT). Temperature is sensitive to the flow of vapor and water, therefore can be used as an indicator of the water movement. Air permeability in fractures can be used to infer the variation of water content in fractures,

assuming that the variation of fracture aperture due to the rock deformation is not significant.

4.1.1 Temperature as a Diagnostic of the Water Movement

In the DST, temperature is measured in the Heated Drift (HD), in the rock mass in resistance temperature device (RTD) boreholes, and in the rock mass in the multiple-point borehole extensiometer (MPBX) boreholes. Because the RTD boreholes are sealed, the temperatures measured in them are more representative of the real temperatures in the rock mass. The temperature measured in the RTD boreholes is used in this discussion of the heat-driven water movements. There are 28 Temperature (RTD) boreholes in the DST (CRWMS, 1998, Table 4-1). Among those, two are parallel to the axis of the Heater Drift, at about 7 m horizontally from the center of HD, and about 3.5 m above the wing heater plane. Twenty six of the Temperature boreholes are radial to the HD. The temporal variation and spatial distribution of the temperature measured in those radial boreholes are used in this discussion of the inferred water movements. In those radial temperature boreholes, RTDs are installed at a spacing of 30 cm and are numbered 1 to 67, starting from near the collar of each borehole.

Figure 30 shows the temperature measured at RTDs 1 to 7 as a function of elapsed days since the heating in borehole#144, which is at 12 m from the bulkhead and oriented 45° away from the Access Observation Drift (AOD). This figure is used as an example to illustrate the effects of heat transfer and moisture movement on the temperature. Temperatures measured in other radial boreholes behavior similar to that shown in Figure 30. The curve RTD-1 in Figure 30 shows the typical temperature-time curve of heat conduction in a partially saturated medium. The temperature rises fast with time at the beginning due to a large thermal gradient between the heat source and RTD-1. The temperature increasing rate decreases with time because of many factors. The major contributing factors include: (1). The thermal gradient decreases with time when the thermal front progresses further from the heat source and expands. (2). Enhanced evaporation of the pore water at elevated temperatures creates a cooling effect. The temperature-time curve shows an inflection point at temperature slightly above 100°C. This increase in the temperature rising rate is caused by factors such as the arrival of additional heating from the wing heaters, decreasing in thermal conductivity of the rock mass due to drying, etc. Later, the temperature increasing rate decreases again because the further decrease of the thermal gradient. The temperature-time curves RTD-2 to RTD-7 show the effect of water movement on the temperature. When more water is available, the effect of water movement, such as evaporation and/or flow, on temperature will be great so that the temperature rising rate is significantly reduced around the boiling point of water. The temperature rising rate may be reduced to near zero if the amount of water is great enough so that rapid evaporation and/or flow of vapor can remove almost all of the energy supplied by the heaters. Later on, when most of the water is removed at temperatures above the boiling point of water, the temperature rises in the same way as that due to thermal conduction only. The number of RTDs in each borehole that involve with such rapid evaporation process, and the duration of each such RTDs to be involved

in such rapid evaporation process are indicators of either the amount of water in the rock mass or the rate that water can be supplied to the region.

The rapid evaporation/boiling process is shown in the temperature measured in all of the temperature boreholes. However, the intensity of the process, the spatial extent of the process, and the temporal duration of such process vary from borehole to borehole. The evaporation process may reach the extent that the temperature in a significant region (involves more than two RTDs) along one borehole may be maintained at a near constant level at any instance. This kind of spatial energy balance occurs in many boreholes with variable extents. This phenomenon was reported in Figure 18 of Thermal Test Progress Report #6 (PR-6) (BSC, 2001).

In some boreholes the amount of water, or the supply of water, is great enough to keep the temperature at certain locality at very close to constant for an extended period of time. This constant level of temperature is defined as the boiling point of water. It was reported in PR-6 that the boiling point of water in some of the temperature boreholes systematically decreased with increasing distance from the heaters (BSC, 2001, Figure 19). Further analysis of the temperature data indicates that this phenomenon occurs in boreholes #137, #138, #144, #158, and #159. This phenomenon of variation of the boiling point of water with distance from the heat source may be due to the variation of ion concentration in the water due to rock-water interaction. This phenomenon seems to be localized. In addition, the range of the boiling point of water varies from borehole to borehole. For example, in borehole #158, which is a vertically up borehole at 23 m from the bulkhead, the boiling point of water ranges from about 97.5 to 101°C; in borehole #159, which is a 45 degree upward borehole at 23 m from the bulkhead, the boiling point of water ranges from about 95.5 to 98.5°C.

The spatial extent and the temporal duration of the rapid evaporation/boiling process is used to assess the availability of water in the regions toward AOD (the region between the HD and the AOD) and from AOD (the region on the other side of the HD). At the mid HD region (at 23 m from the bulkhead) the to-AOD region seems to have more water than the from-AOD region. But near the ends of the HD (at 12 m from the bulkhead and 39 m from the bulkhead) the from-AOD region seems to have more water than the to-AOD region. These are illustrated by the following figures.

Figures 31, 32, 33, and 34 show the temperature-time curves in boreholes #138 and #144 respectively. Both boreholes #138 and #144 are the 45-degree upward boreholes at about 12 m from the bulkhead. Borehole #138 is in the to-AOD region; borehole #144 is in the from-AOD region. These figures show that more RTDs in borehole #144 (RTD-7 and above, as shown in Figure 32) were involved in the rapid evaporation process than in borehole #138 (RTD-14 and above, as shown in Figure 31). And the duration of the process in borehole #144 (e.g. more than 360 days at RTD-21, as shown in Figure 33) is longer than that in borehole #138 (e.g. less than 200 days at RTD-21, as shown in Figure 32). Figures 35 to 39 show the temperature-time curves in borehole #140 and #142 respectively. Both boreholes #140 and #142 are the 45-degree downward boreholes at 12 m from the bulkhead. Borehole #140 is in the to-AOD region; borehole #142 is in the

from-AOD region. These figures show that the number of RTDs in borehole #140 (RTD-5 to RTD-9, as shown in Figures 35 and 36) involved in the rapid evaporation process are fewer than that in borehole #142 (RTD-19 to RTD-30, as shown in Figures 37 to 39). In summary, at 12 m from the bulkhead, the region to-AOD has less water available to sustain the rapid evaporation process than the region from-AOD.

Figures 40 to 45 show the temperature-time curves in borehole #159 and #165. Both boreholes #159 and #165 are 45-degree upward boreholes at about 23 m from the bulkhead. Borehole #159 is in the to-AOD region; borehole #165 is in the from-AOD region. These figures show that more RTDs in borehole #159 (RTD-21 to RTD-36, as shown in Figures 40 to 43) than in borehole #165 (RTD-21 to RTD-29, as shown in Figures 44 and 45) are involved in the rapid evaporation/boiling process. This is an indication that more water was available in the upper to-AOD region than in the upper from-AOD region at 23 m from the bulkhead. Figures 17 to 23 show the temperature-time curves in boreholes #161 and #163, both are 45-degree down-ward boreholes at about 23 m from the bulkhead. There are more RTDs in borehole #161 (as shown in Figures 46 to 49) than in borehole #163 (as shown in Figures 50 to 52) involved in the rapid evaporation process. This is an indication that below the heater plane at 23 m from the bulkhead, the to-AOD region seems have more water available than in the from-AOD region. In summary, at 23 m from the bulkhead, the temperature-time curves show that there is more water available in the to-AOD region than in the from-AOD region.

At 39 m from the bulkhead the temperature-time curves are shown in Figures 53 to 67. In the upper region, there seem to have fewer RTDs in borehole #171 (as shown in Figures 53 to 55) than in borehole #175 (as shown in Figures 56 to 59) involved in the rapid evaporation/boiling process. Borehole #171 is in the to-AOD region, while borehole #175 is in the from-AOD region. In other words, in the region above the heater plane at 39 m from the bulkhead, the to-AOD region seems to have less water available than the from-AOD region. On the other hand, below the heater plane, there are more RTDs in borehole #172 (as shown in Figures 60 to 64) than in borehole #174 (as shown in Figures 65 to 67) involved in the rapid evaporation/boiling process. Borehole #172 is in the to-AOD region; and borehole #174 is in the from-AOD region. Therefore, in the region below the heater plane at 39 m from the bulkhead, the to-AOD region seems to have more water available than the from-AOD region.

In summary, the availability of water to sustain a rapid evaporation/boiling process varies with distance from the bulkhead. The availability of water depends on initial moisture content and the rate at which water can be supplied to a region. In the region above the heater plane, less water was available in the to-AOD region than in the from-AOD region at 12 and 39 m from the bulkhead. The reverse is true at 23 m from the bulkhead. In the region below the heater plane, more water was available in the to-AOD region than in the from-AOD region at 23 and 39 m from the bulkhead. The reverse is true at 12 m from the bulkhead. Some sort of water movement in a scale greater than the DST may have caused this variation of the availability of water.

4.1.2 Integrated Interpretation of Geophysical Methods of Monitoring Water Movement

The geophysical methods used to monitor the spatial distribution and the temporal variation of moisture content are ground-penetrating radar (GPR), electrical resistance tomography (ERT) and neutron logging. Water movement is inferred from the measured spatial distribution and temporal variation of the moisture content. In this report all of the geophysical measurement results are presented as referenced to the pre-heat moisture content. Therefore only the changes in the moisture content due to the heating is presented. The boreholes used for conducting GPR, ERT, and neutron logging are listed in CRWMS (1998). At the Thermal Test Workshop the GPR results were not available to be incorporated with the results of ERT and neutron logging yet, therefore were presented separately.

Ground-Penetrating Radar Results

GPR in the DST is conducted in the neutron logging boreholes originated from the AOD, which are boreholes #64 to #68, and boreholes #47 to #51. As shown in CRWMS (1998), boreholes #47 to #51 form an array intersecting the HD at a distance about 6.4 m from the bulkhead, and boreholes #64 to #68 intersect the HD at about 26.5 m from the bulkhead. Generally speaking, the GPR results show drying in regions near the heaters, and increasing moisture content outside of the drying regions. This is in general agreement with the ERT and the neutron logging results, as will be shown later. Due to the high temperature, GPR in boreholes #64 to #68 were not conducted after October 27, 1999. This is unfortunate because boreholes #64 to #68 covers the mid portion of the HD, which is influenced less by end effects.

Figures 68 to 70 show some examples of the GPR results. Figure 68 shows the GPR results measured in boreholes #65 to #68 on October 27, 1999. This was the last measurement conducted in this array of boreholes. The circle in this figure represents the HD. Borehole #65 is the highest borehole in this figure, and borehole #68 is the lowest one. There was no measurement conducted in borehole #64, which is the highest borehole in this array, and is above borehole #65. Figure 68 illustrates that the heating moves water radially from the heat source. The image in Figure 68 is the changes in saturation, from +0.3 to -0.6. Figures 69 and 70 show the variation of the change in saturation between April 14, 2000 and February 6, 2001, as measured by GPR in boreholes #49 to #51. Borehole #49 is immediately above the HD, which is represented by a circle, and boreholes #50 and #51 are below the HD. There was no measurement conducted in boreholes #47 and #48, which are above borehole #49. The changes in the saturation change between 4/14/00 (Figure 69) and 2/06/01 (Figure 70) are the increase in the drying region to the side below the HD, decreasing the extent of increasing saturation directly below the HD, and increasing the region of increasing saturation near the AOD. The GPR data seem to show a greater extent of drying than the neutron data. Because of the sparse spatial coverage of the GPR measurement, not much more information about the water movement can be obtained from the measurements.

ERT and Neutron Logging Results

ERT is conducted in 8 planes in the DST: two vertical planes from the AOD to the HD intersecting the HD at 4.6 and 25 m from the bulkhead, three vertically up planes parallel to the HD axis, and three vertically down planes parallel to the HD axis. The three vertically up planes origin at the crown of the HD, and cover the distance ranges 2.7 to 12, 12 to 23 and 23 to 39 m from the bulkhead respectively. The three vertically down planes origin at the invert of the HD, and cover the same distances as the vertically up planes. As shown in CRWMS (1998), there are twelve neutron boreholes in the DST. Ten of those boreholes (#47 to #51, and #64 to #68) origin from the AOD, and form two vertical arrays intersecting the HD at 6.4 and 26.5 m from the bulkhead respectively. The boreholes in these two arrays are shared by GPR, as mentioned above. Neutron logging is also conducted in two horizontal boreholes parallel to the HD axis, at about 3.5 m above the mid wing heater plane (holes #79 and #80). In this analysis, the ratio of the ERT and the neutron data obtained at about the same time, with respect to their pre-heat data, are plotted in a same figure. Because the neutron logging is more frequent than the ERT, neutron data obtained at about the same time as the ERT is selected to be plotted with the ERT data. The result ratio images are shown in Figures 71 to 87. In these figures a ratio 1 means no change in the moisture content; a ratio of greater than 1 means increasing in moisture content; and a ratio of less than 1 means losing moisture. It should be noted that the neutron borehole arrays and the ERT planes origin from the AOD are off-set by about 1.5 to 1.8 m along the AOD axis. A neutron borehole array is about 1.5 to 1.8 m farther away from the bulkhead than its nearby ERT plane.

Figures 71 to 87 show both spatial and temporal variations of the moisture ratio as measured by ERT and neutron logging, as the heating goes on. Early in the heating phase an extended drying region developed in the transverse ERT plane (the ERT plane originates at the AOD and perpendicular to the HD) closer to the bulkhead (Figures 71 and 72). This may be related to the moisture loss through the bulkhead, because the temperature in the transverse plane at mid point of the HD is greater than that closer to the bulkhead. This drying region extended by 3/16/98 (Figure 72), and the moisture content increased in regions above and below it. Both ERT and neutron show the increase in the moisture content. By 4/22/98 (Figure 73) the drying became more normal as would be expected from the heating. In other words, by 4/22/98 the region at the mid point of the HD showed more drying than that closer to the bulkhead, as would be expected. The moisture in the regions both above and below the heaters are increased. But the region below the heaters shows greater increase in moisture. This condition was maintained for a couple of months until 7/22/98, when the region above the heaters at the mid point of the HD seemed to have greater increase in moisture (Figures 75).

Later when the drying near the heaters progressed, the increase of moisture became evident everywhere outside of the drying region, with especially significant increase in moisture in the region below the heaters closer to the bulkhead (Figures 76 to 81). Then by 6/1/99 (Figure 82) most of the increasing moisture in the region between the AOD and the HD at 4.6 m from the bulkhead was gone; increasing moisture still existed in the region above the wing heaters, between the AOD and the HD at 25 m from the bulkhead; and increasing moisture also existed in the regions directly above and below the HD.

These conditions stayed through 9/29/99 (Figure 83). By 11/02/99 (Figure 84) the moisture in the regions above and below the wing heaters, between the AOD and the HD had increased; the same occurred in the region directly below and above the HD, at a distance greater than 25 m from the bulkhead. By 1/21/00 (Figure 85) the increasing moisture in the region between the AOD and the HD at 25 m from the bulkhead was gone; the moisture increase above and below the HD still existed; and there was an increase in moisture below the wing heater at 4.6 m from the bulkhead. By 9/26/00 and through 2/5/01 (Figures 86 and 87) the only region where increasing moisture existed was above the HD at a distance greater than 25 m from the bulkhead.

The variations of the moisture content with respect time as shown by the ERT/neutron data, and the spatial variation in the moisture as indicated by the temperature data (as shown above) may be due to heterogeneity in the rock mass or a larger scale moisture movement.

4.1.3 References

BSC, 2001, Thermal Test Progress Report #6, Bechtel SAIC Company, LLC, Las Vegas, NV 89144.

CRWMS, 1998, Drift Scale Test As-Built Report, BAB000000-01717-5700-00003, TRW Environmental Safety System Inc. Las Vegas, NV.

Temperature in hole#144, at 12 m from the bulkhead, 45 degree from AOD.

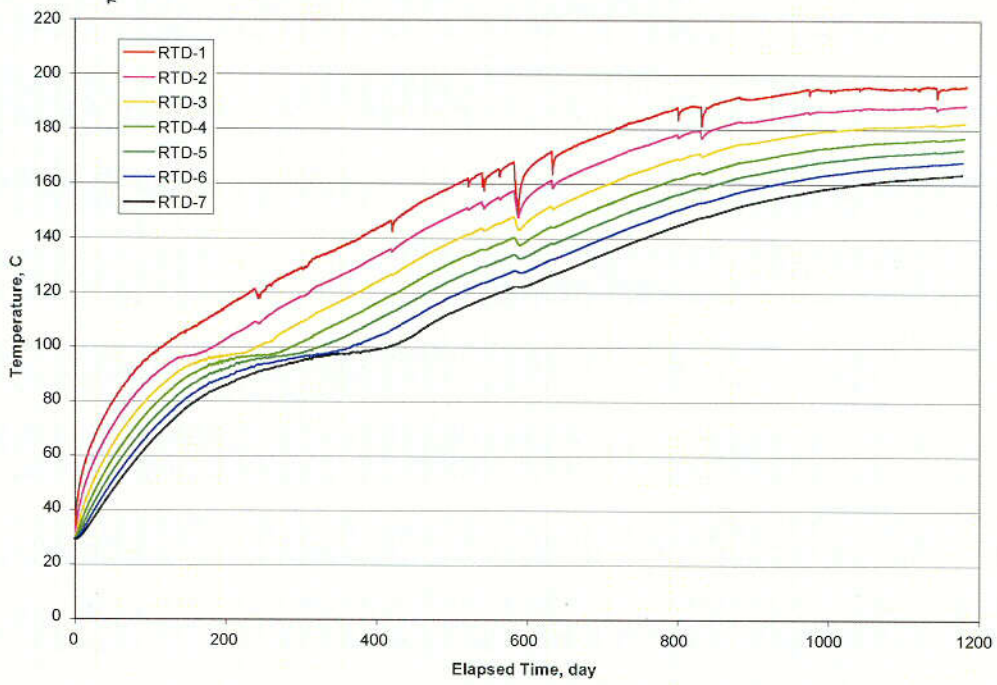


Figure 30. Temperature at RTDs 1-7 in borehole #144 as a function of time.

Temperature in hole#138, at 12 m from the bulkhead, 45 degree to AOD.

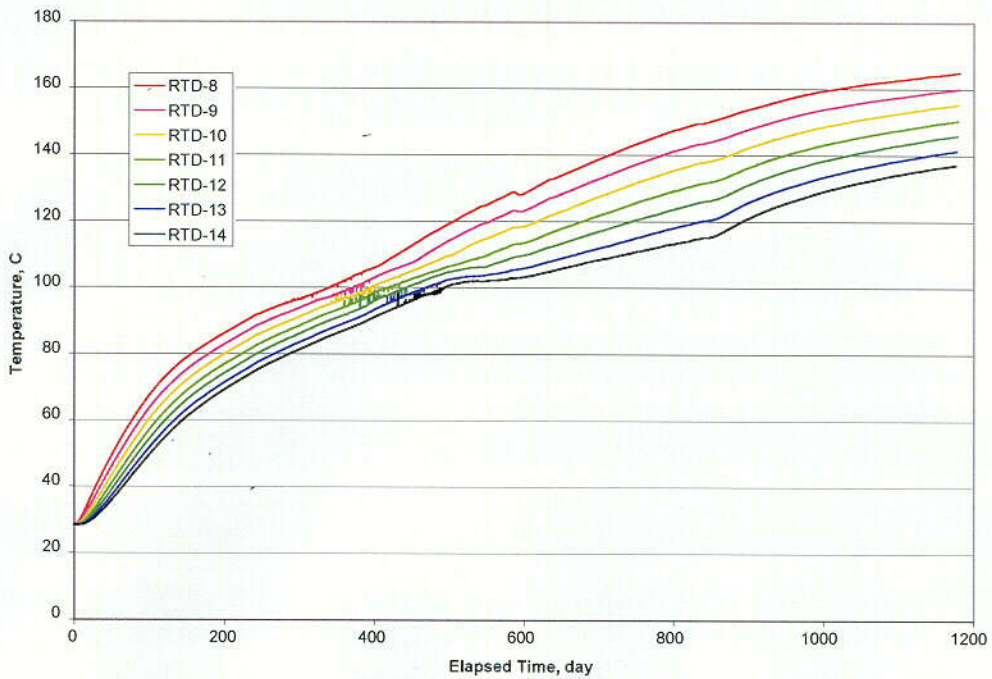


Figure 31. Temperature-time curves in borehole #138 show that rapid evaporation process starts at RTD-14.

C08

Temperature in hole#138, at 12 m from the bulkhead, 45 degree to AOD.

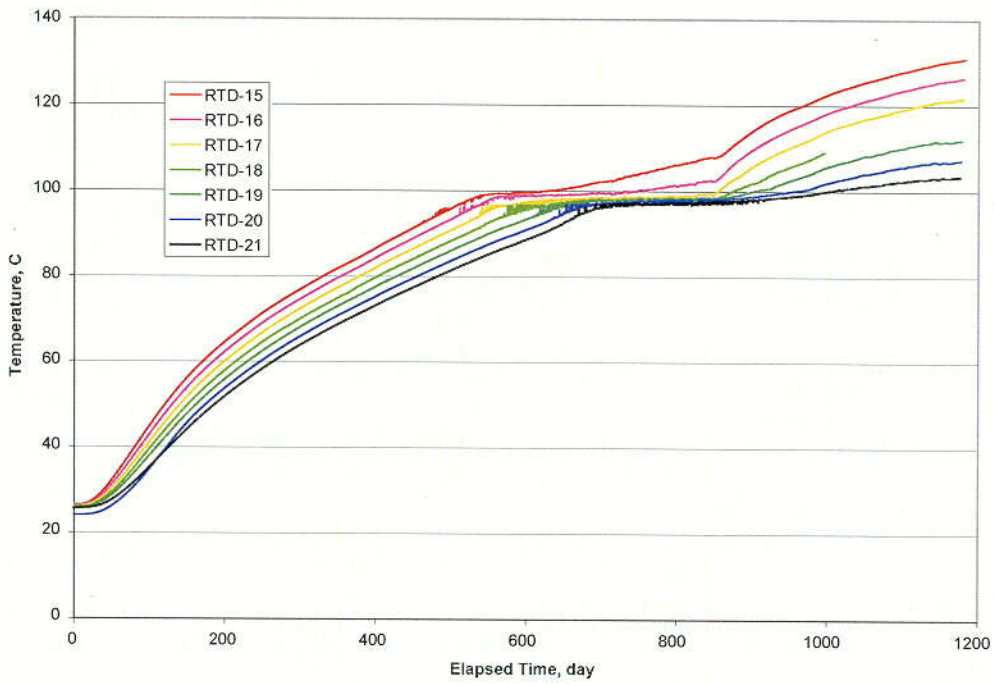


Figure 32. The temperature-time curves in borehole #138 show the duration of the rapid evaporation process. At RTD-21 the duration is almost 200 days.

Temperature in hole#144, at 12 m from the bulkhead, 45 degree from AOD.

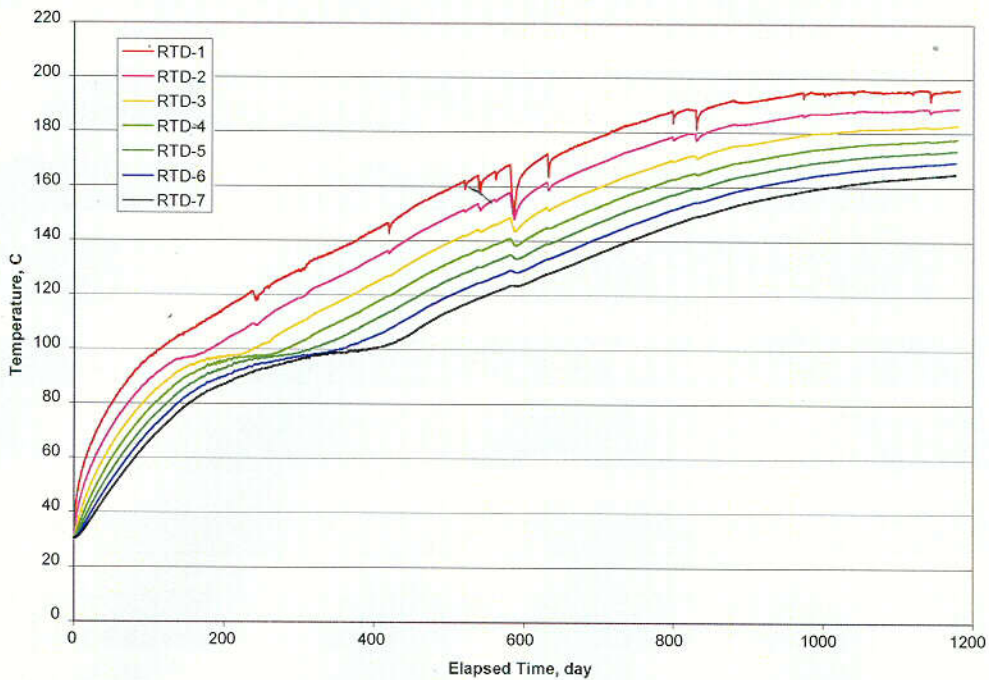


Figure 33. The temperature-time curves in borehole #144 show that the rapid evaporation process starts at RTD-7.

Temperature in hole#144, at 12 m from the bulkhead, 45 degree from AOD.

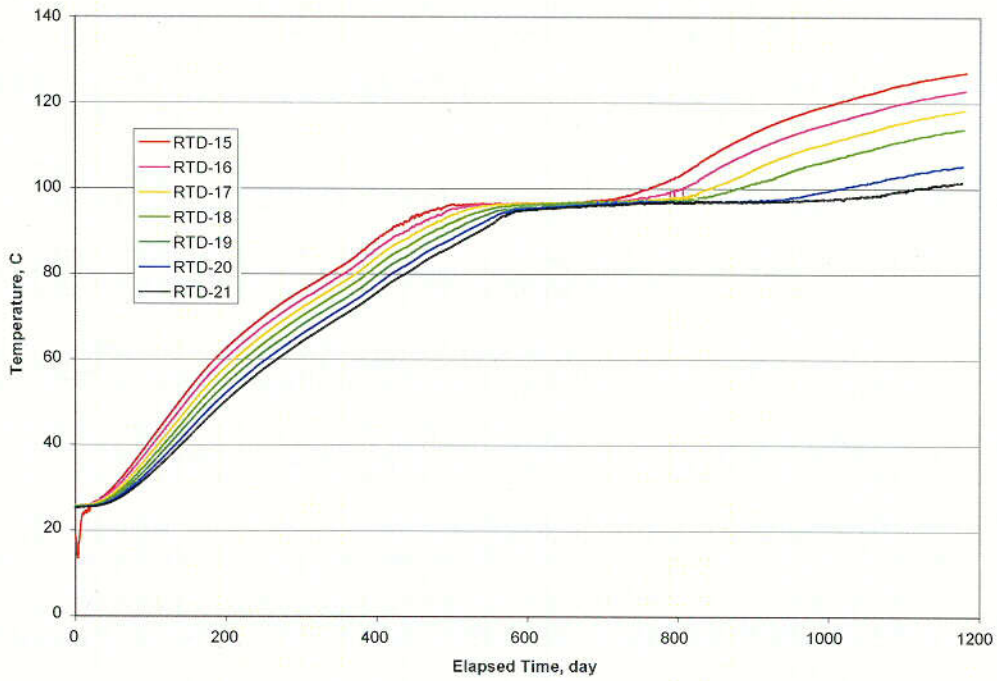


Figure 34. The temperature-time curves in borehole #144 show the duration of the rapid evaporation process at RTD-21 is greater than 360 days.

Temperature in hole#140, at 12 m from the bulkhead, -45 degree to AOD.

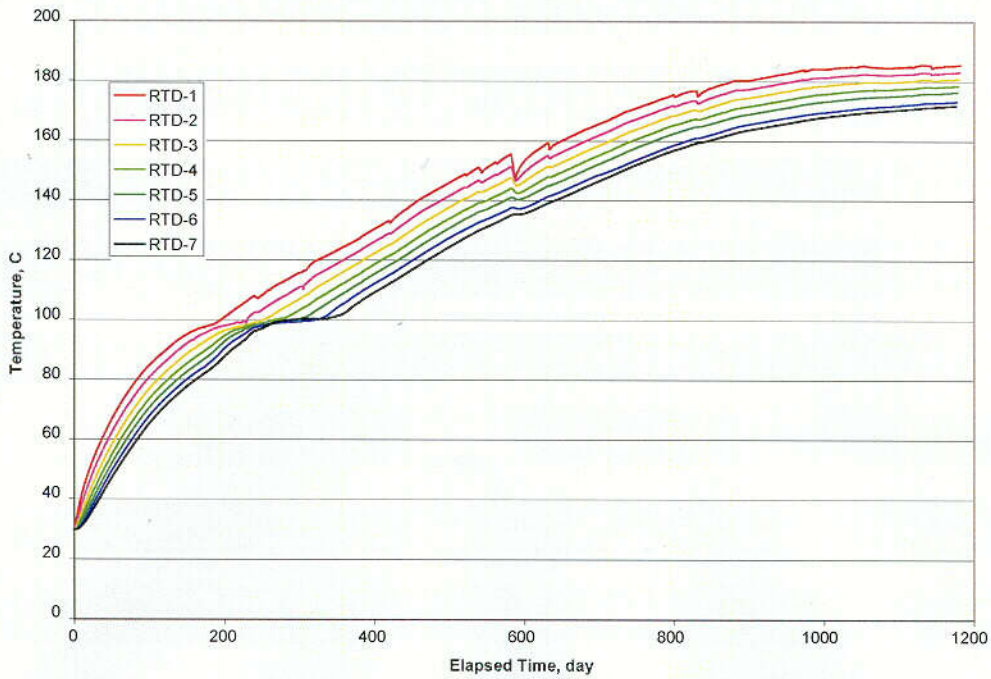


Figure 35. The temperature-time curves in borehole #140 show that the rapid evaporation process starts at RTD-5.

C10

Temperature in hole#140, at 12 m from the bulkhead, -45 degree to AOD.

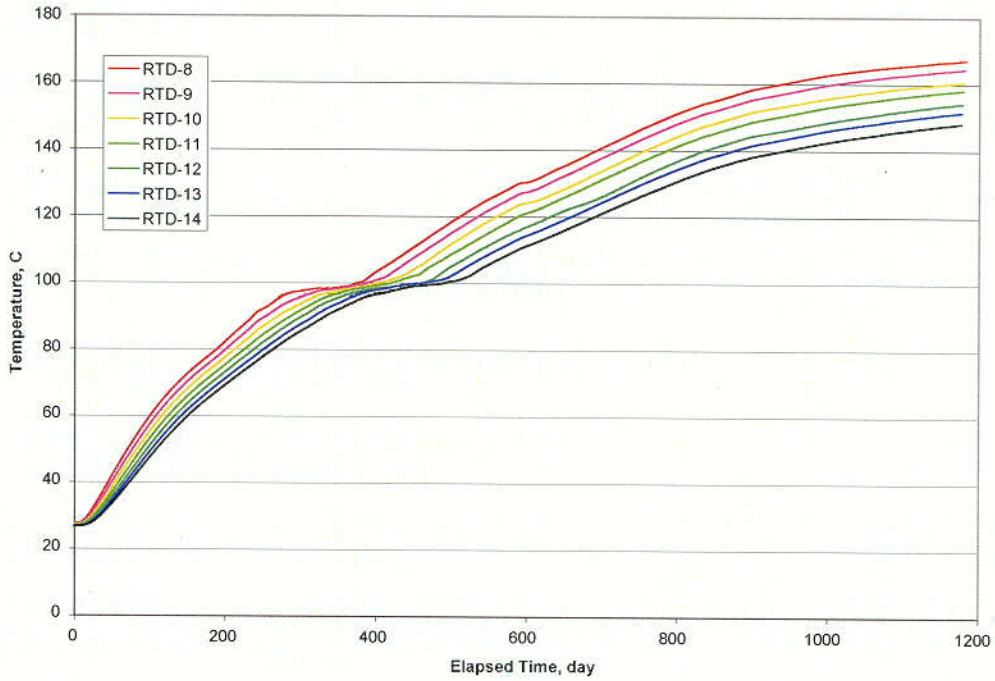


Figure 36. The temperature-time curves in borehole #140 show that the almost constant temperature curves end at RTD-9.

Temperature in hole#142, at 12 m from the bulkhead, -45 degree from AOD.

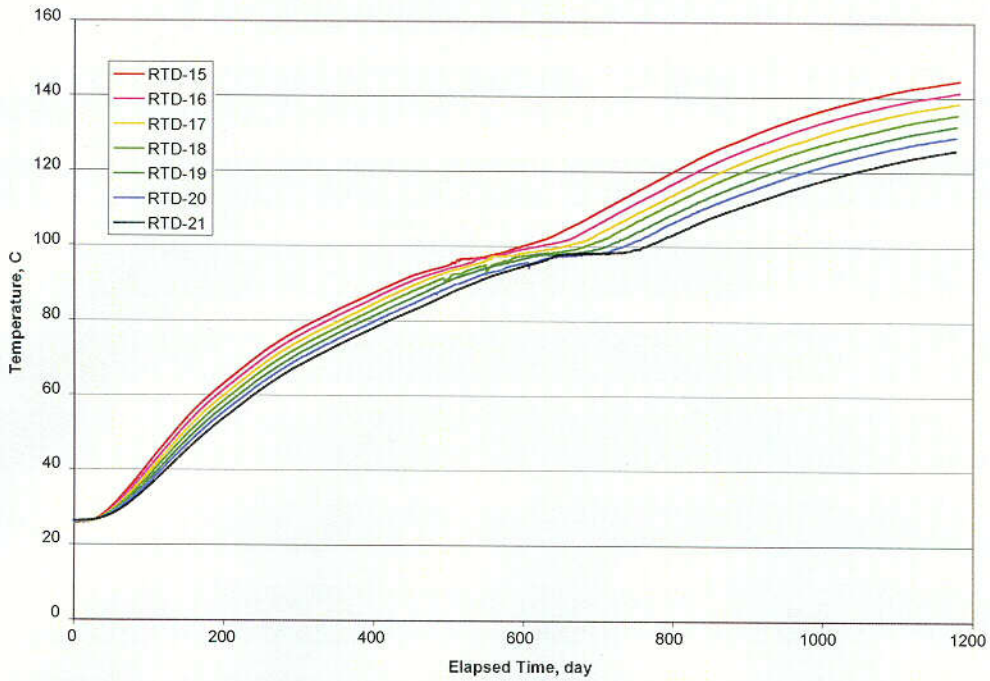


Figure 37. The temperature-time curves in borehole #142 show that the almost constant temperature starts at RTD-19.

Temperature in hole#142, at 12 m from the bulkhead, -45 degree from AOD.

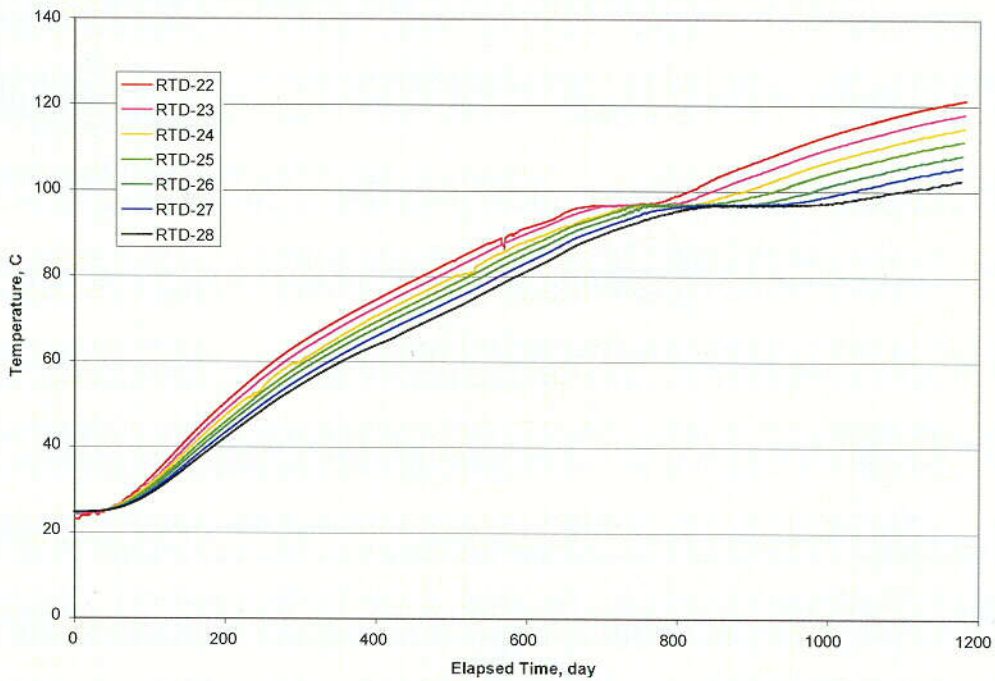


Figure 38. The temperature-time curves in borehole #142 show the well-defined almost constant temperature at RTD-22 to RTD-28.

Temperature in hole#142, at 12 m from the bulkhead, -45 degree from AOD.

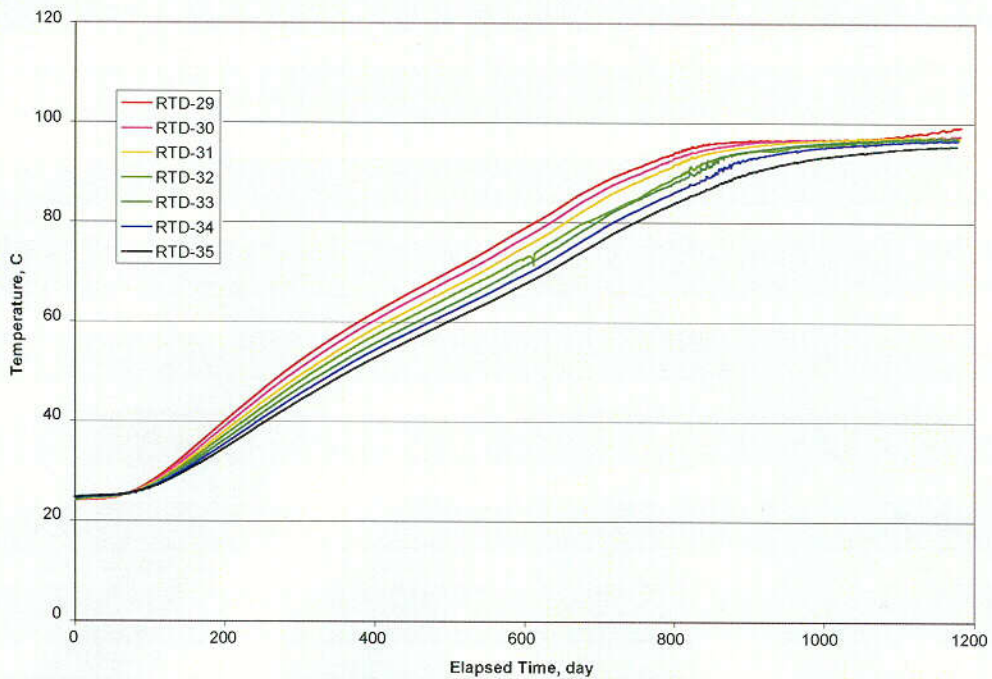


Figure 39. The temperature-time curves in borehole #142 show the almost constant temperature occurs at RTD-29 and RTD-30 so far, and may be more later.

Temperature in hole#159, at 23m from the bulkhead, 45 degree to AOD.

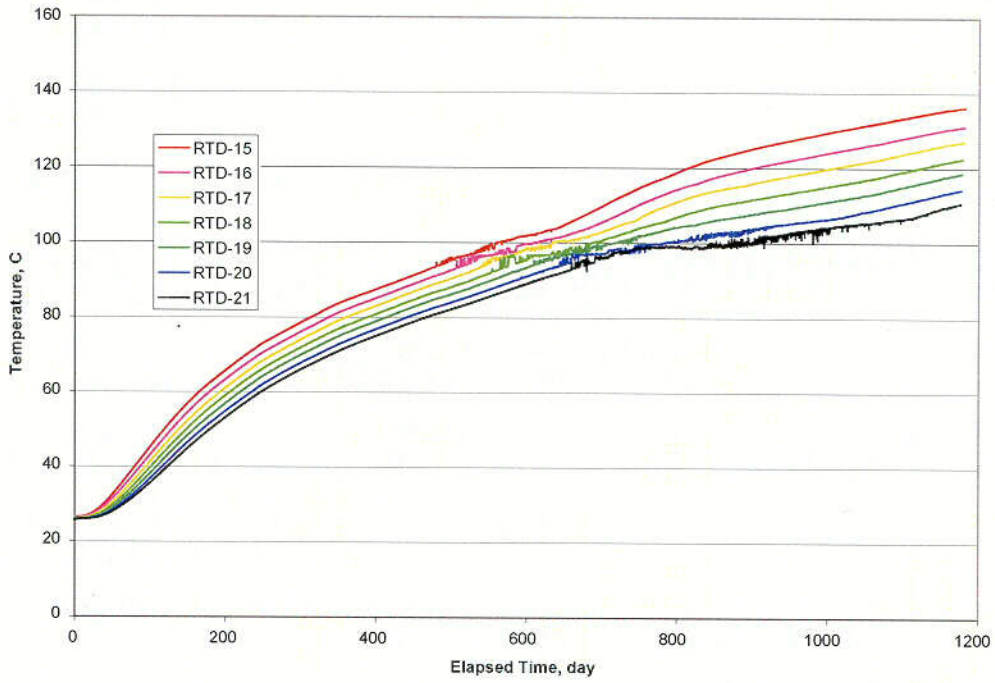


Figure 40. The temperature-time curves in borehole #159 show that the rapid evaporation process starts at RTD-21.

Temperature in hole#159, at 23 m from the bulkhead, 45 degree to AOD.

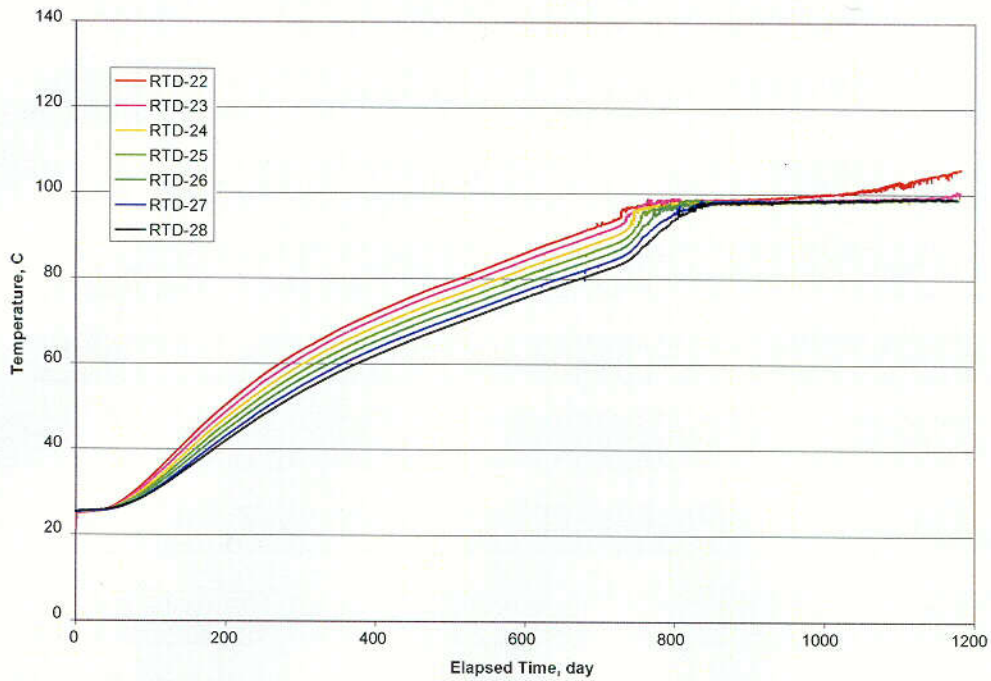


Figure 41. Well-defined almost constant temperature curves at RTD-22 to RTD-28 in borehole #159.

Temperature in hole#159, at 23 m from the bulkhead, 45 degree to AOD.

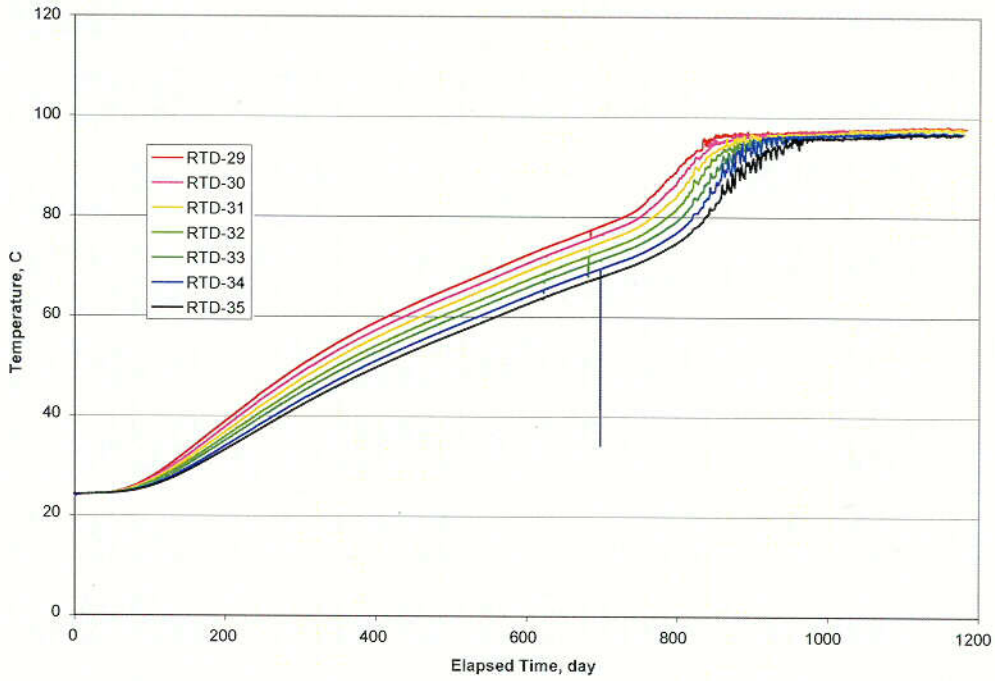


Figure 42. The well-defined almost temperature curves in borehole #159 occur at RTD-29 to RTD-35.

Temperature in hole#159, at 23 m from the bulkhead, 45 degree to AOD.

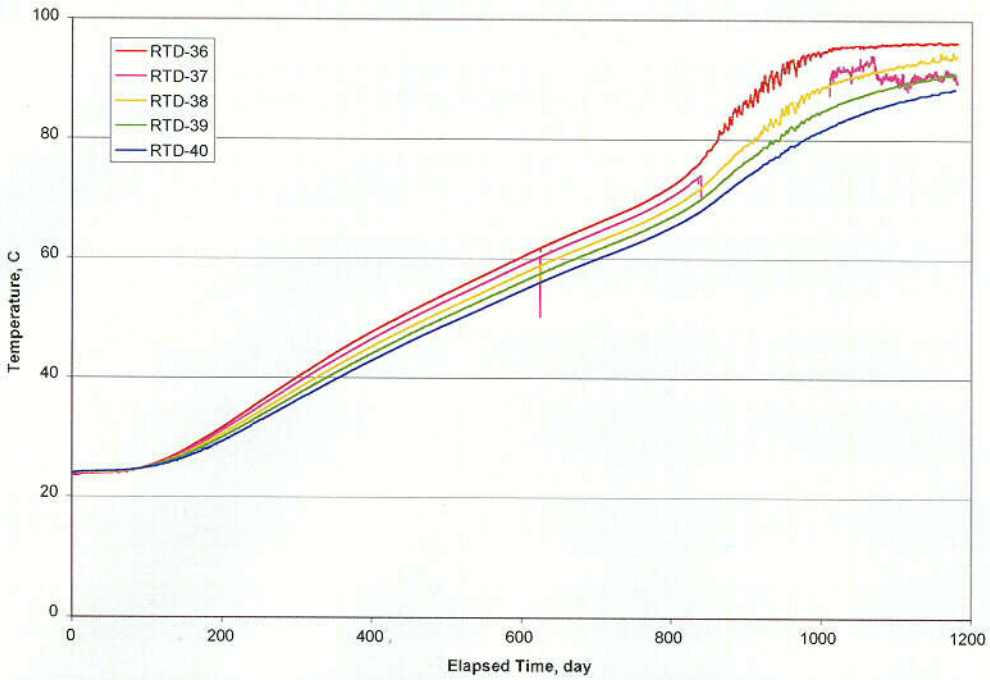


Figure 43. The well-defined almost constant temperature curve in borehole #159 occurs at RTD-36, and may be more later.

Temperature in hole#165, at 23 m from the bulkhead, 45 degree from AOD.

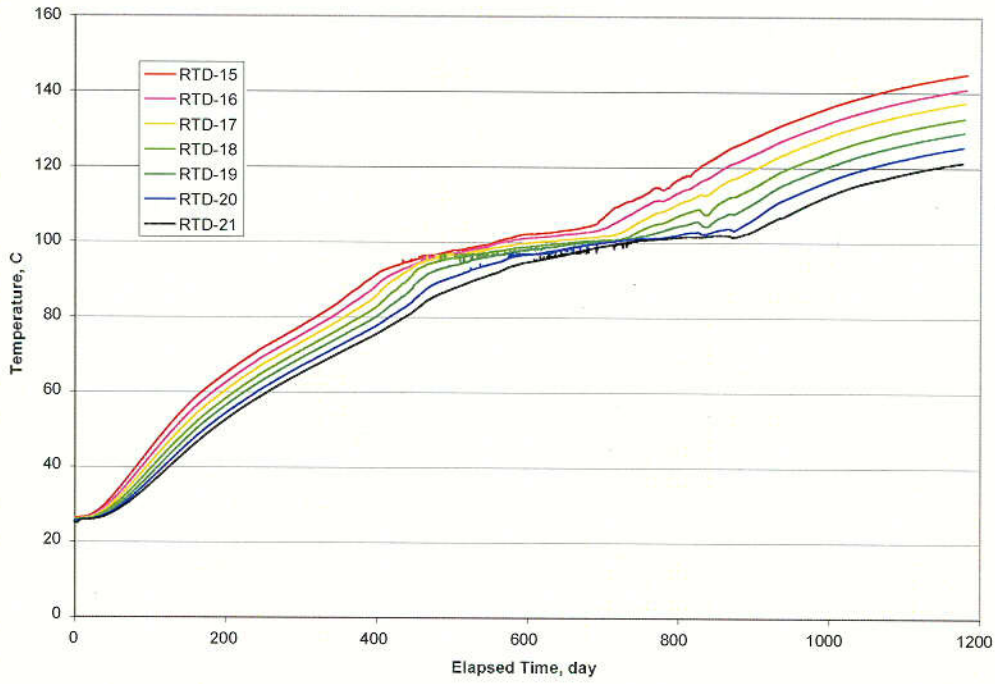


Figure 44. The rapid evaporation process in borehole #165 may be developing at RTD-21, but the temperature is not quite almost constant.

Temperature in hole#165, at 23 m from the bulkhead, 45 degree from AOD.

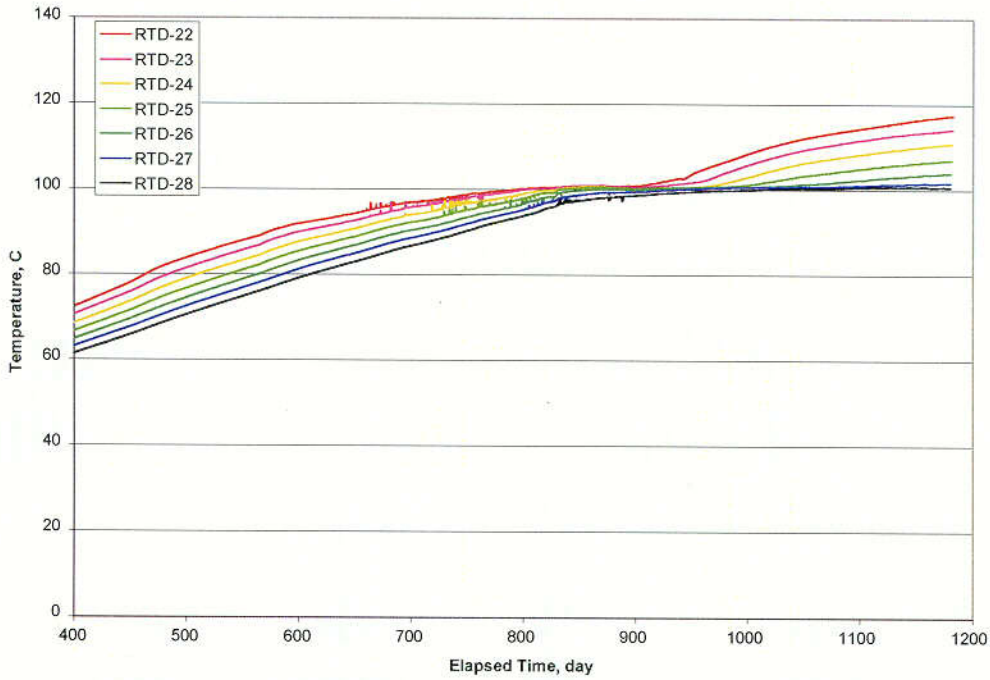


Figure 45. The temperature-time curves in borehole #165 are not as flat as those in borehole #159.

Temperature in hole#161, at 23 m from the bulkhead, -45 degree to AOD.

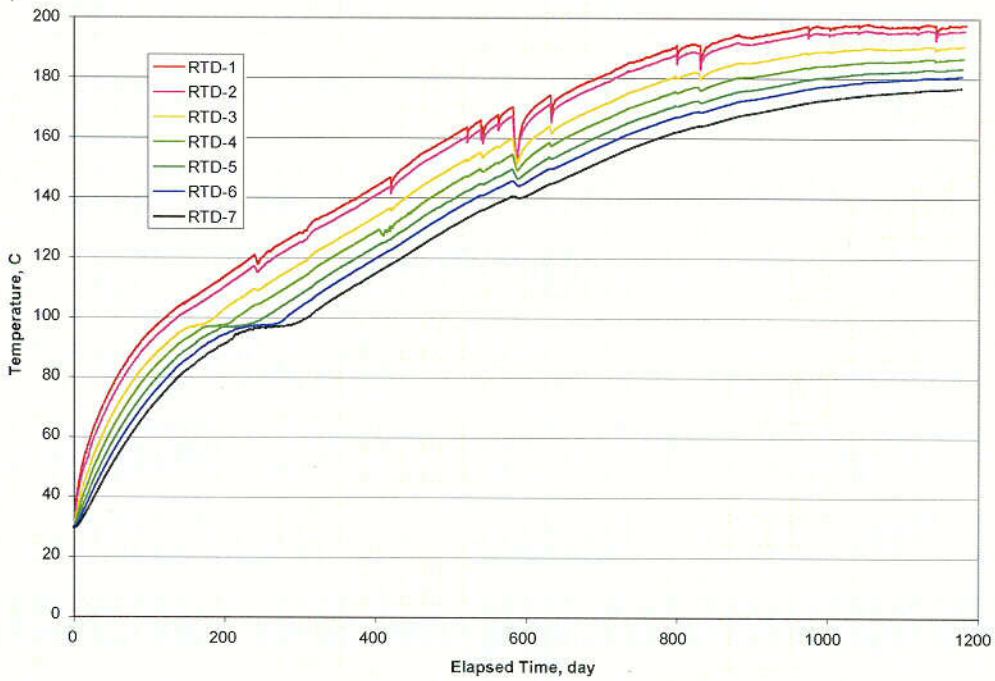


Figure 46. The temperature-time curves in borehole #161 show that the almost constant temperature occurs at RTD-6 and RTD-7.

Temperature in hole#161, at 23 m from the bulkhead, -45 degree to AOD.

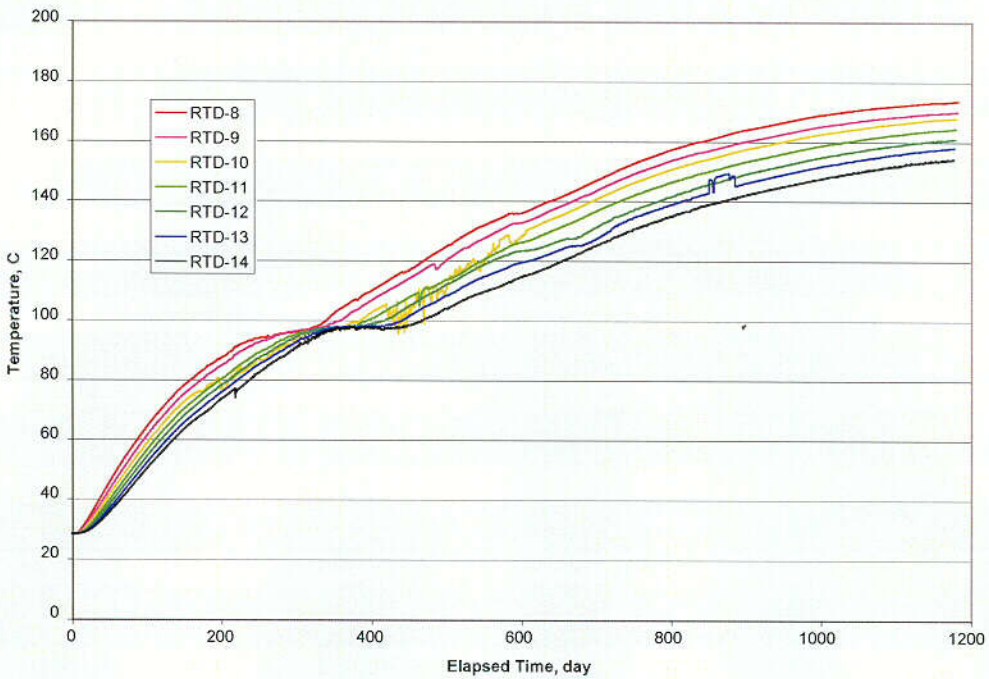


Figure 47. The almost flat temperature-time curves in borehole #161 occur at RTD-11 to RTD-14.

Temperature in hole#161, at 23 m from the bulkhead, -45 degree to AOD.

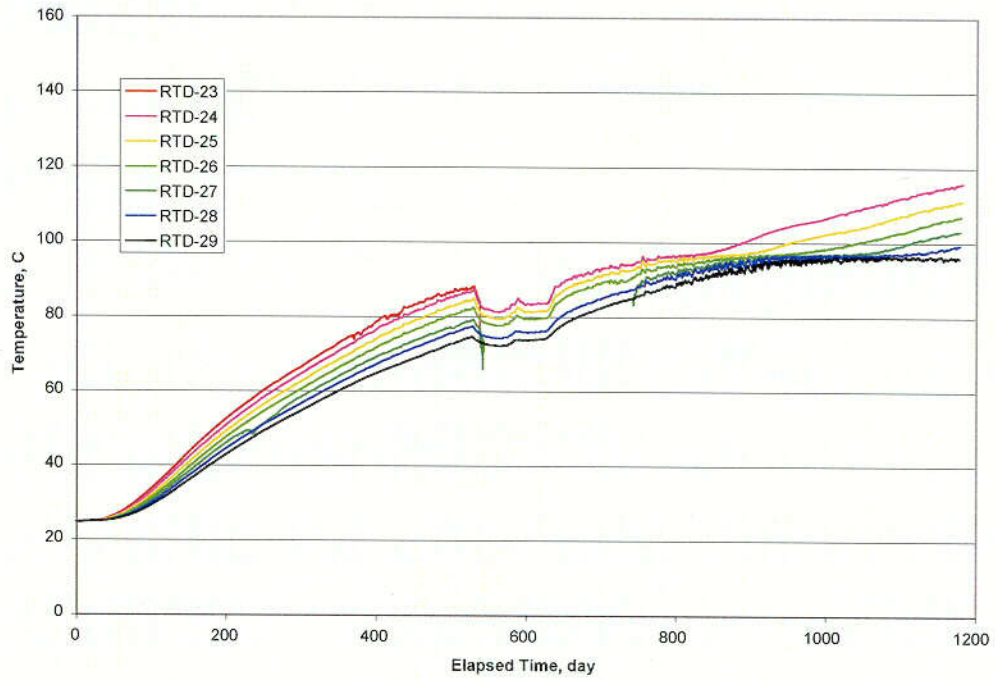


Figure 48. The almost constant temperature in borehole #161 occurs at RTD-16 to RTD-22.

Temperature in hole#161, at 23 m from the bulkhead, -45 degree to AOD.

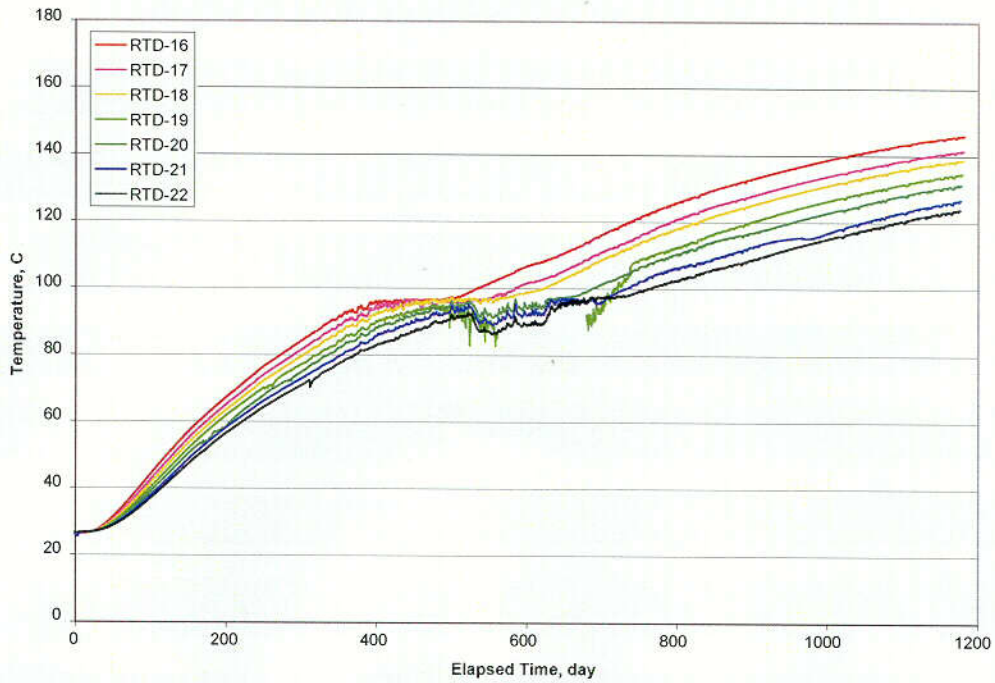


Figure 49. The almost constant temperature in borehole #161 occurs at RTD-27 to RTD-29.

Temperature in hole#163, at 23 m from the bulkhead, -45 degree from AOD.

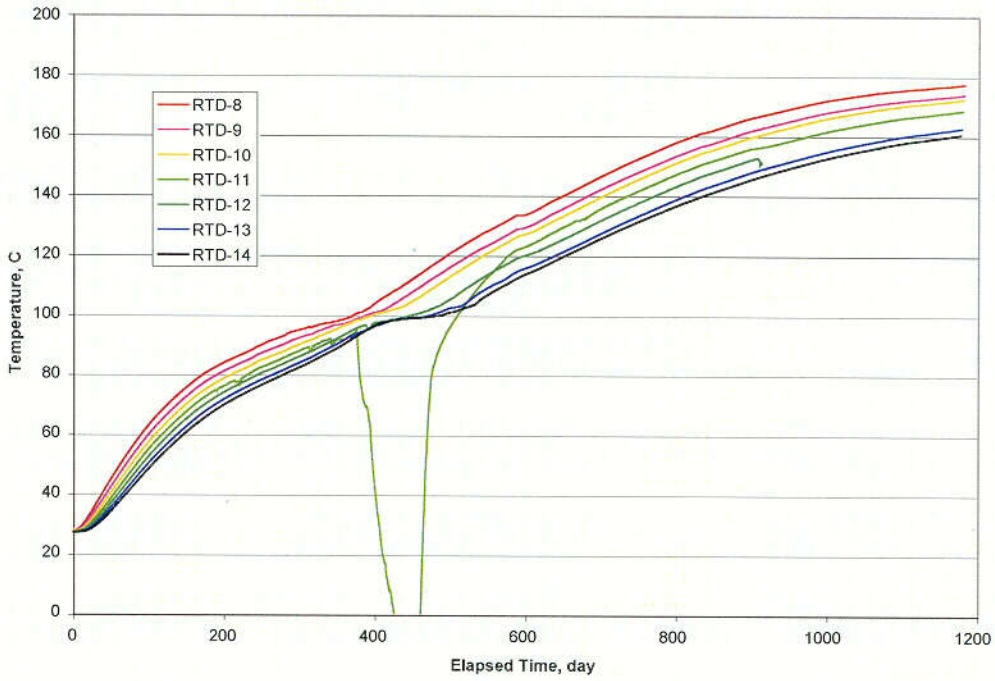


Figure 50. Rapid-evaporation process in borehole #163 develops at RTD-14. But the temperature-time curve is not very flat.

Temperature in hole#163, at 23 m from the bulkhead, -45 degree from AOD.

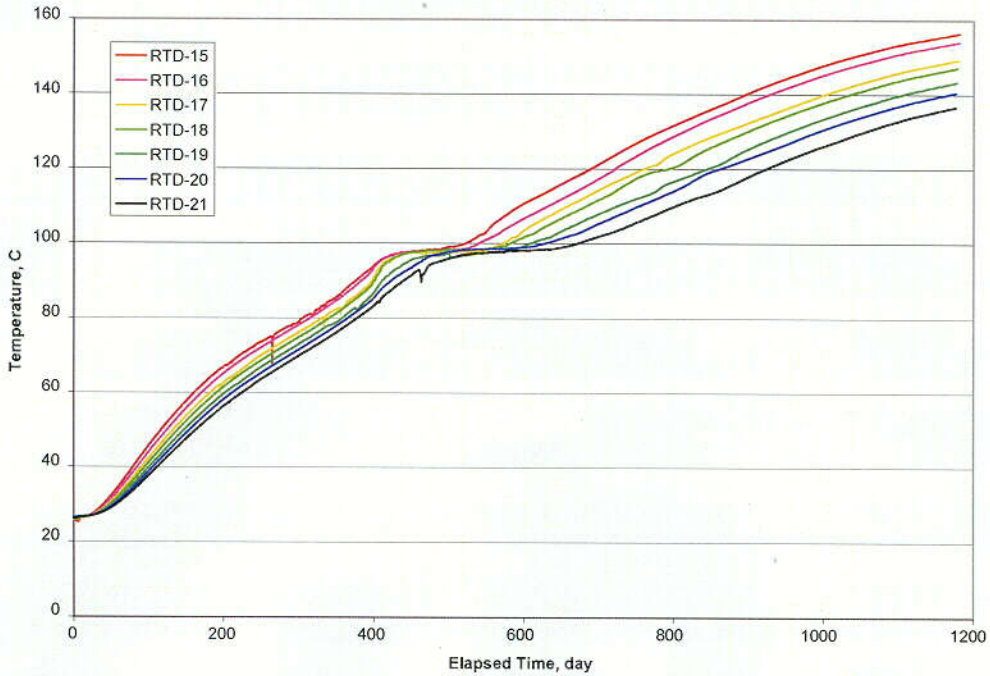


Figure 51. The temperature-time curves in borehole #163 are quite flat at RTD-16 to RTD-21.

Temperature in hole#163, at 23 m from the bulkhead, -45 degree from AOD.

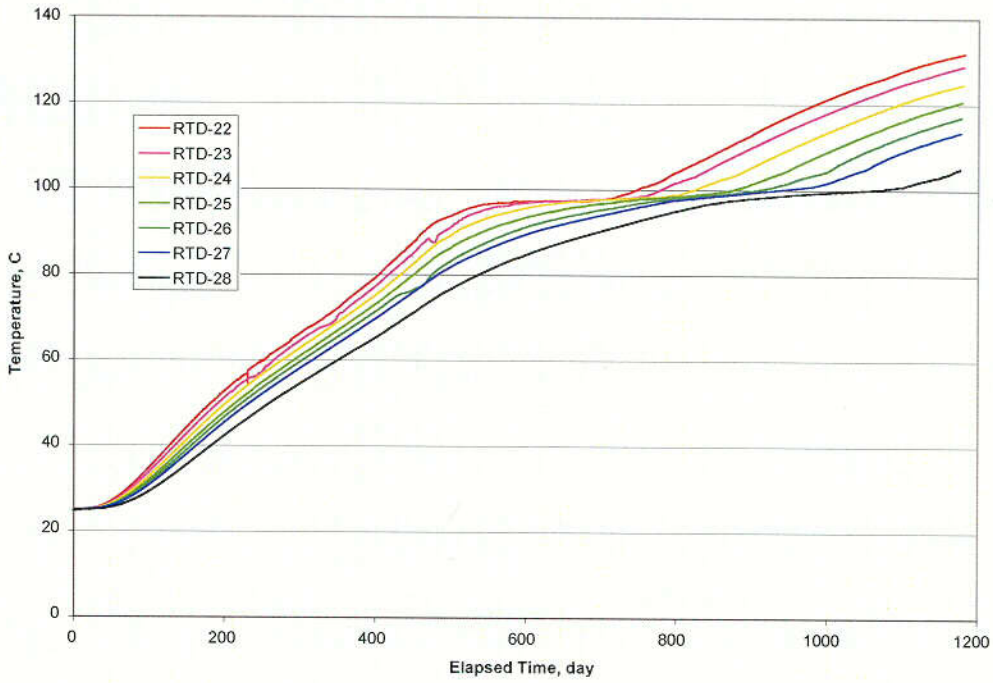


Figure 52. The temperature-time curves in borehole #163 at RTD-22 and RTD-23 have almost flat segments.

Temperature in hole#171, at 39m from the bulkhead, 45 degree to AOD.

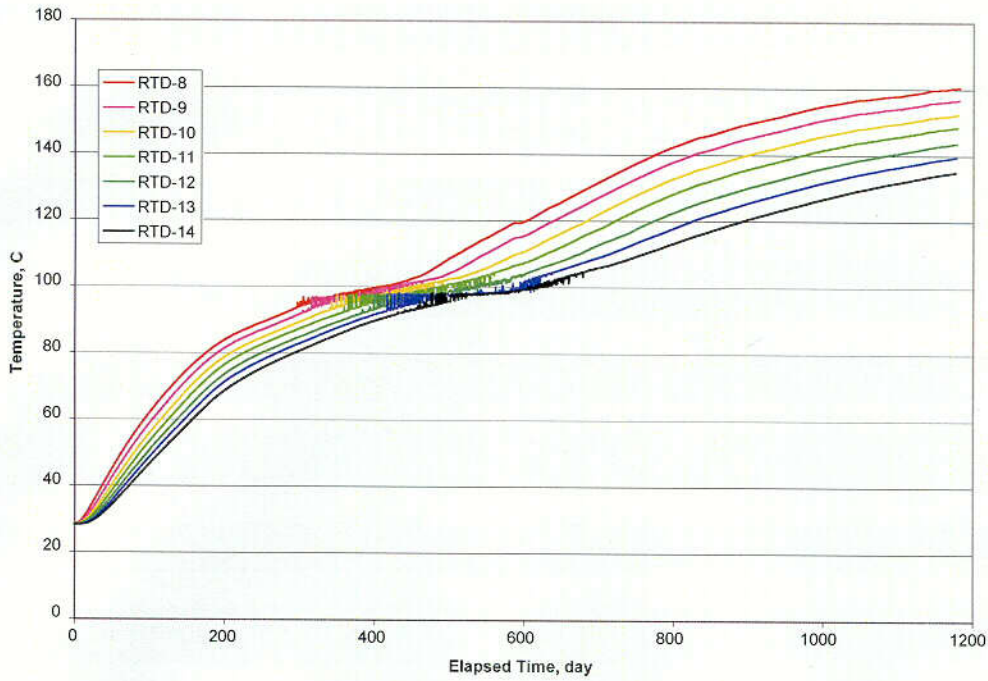


Figure 53. The temperature-time curves in borehole #171 show that the rapid evaporation process starts at RTD-13.

Temperature in hole#171, at 39m from the bulkhead, 45 degree to AOD.

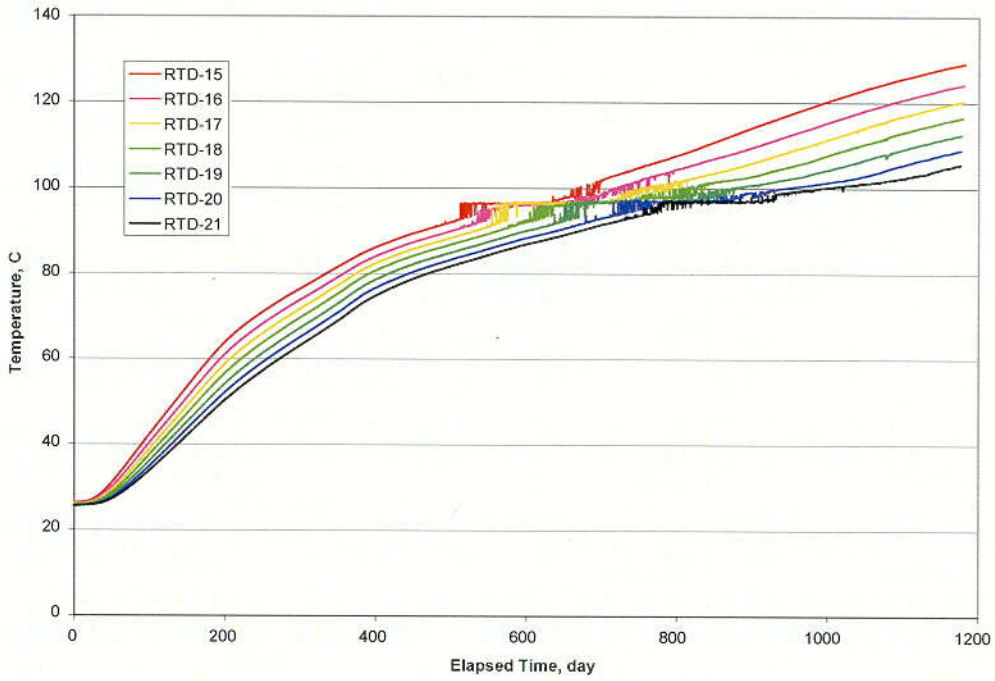


Figure 54. The temperature-time curves in borehole #171 at RTD-15 to RTD-21 have flat segments.

Temperature in hole#171, at 39m from the bulkhead, 45 degree to AOD.

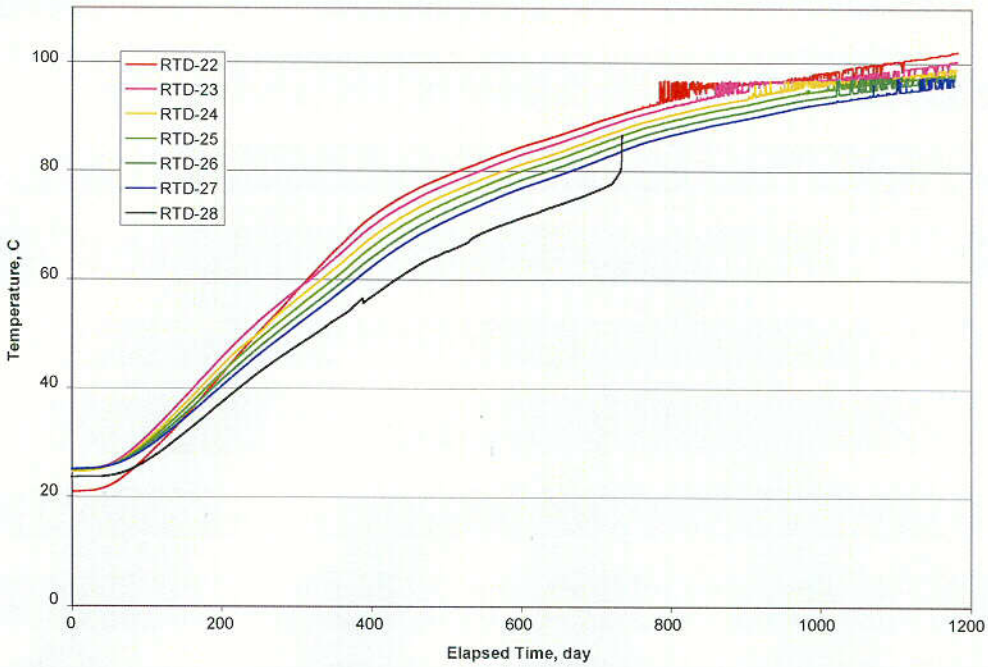


Figure 55. The temperature-time curves in borehole #171 at RTD-22 and RTD-23 show almost constant temperature periods.

Temperature in hole#175, at 39m from the bulkhead, 45 degree from AOD.

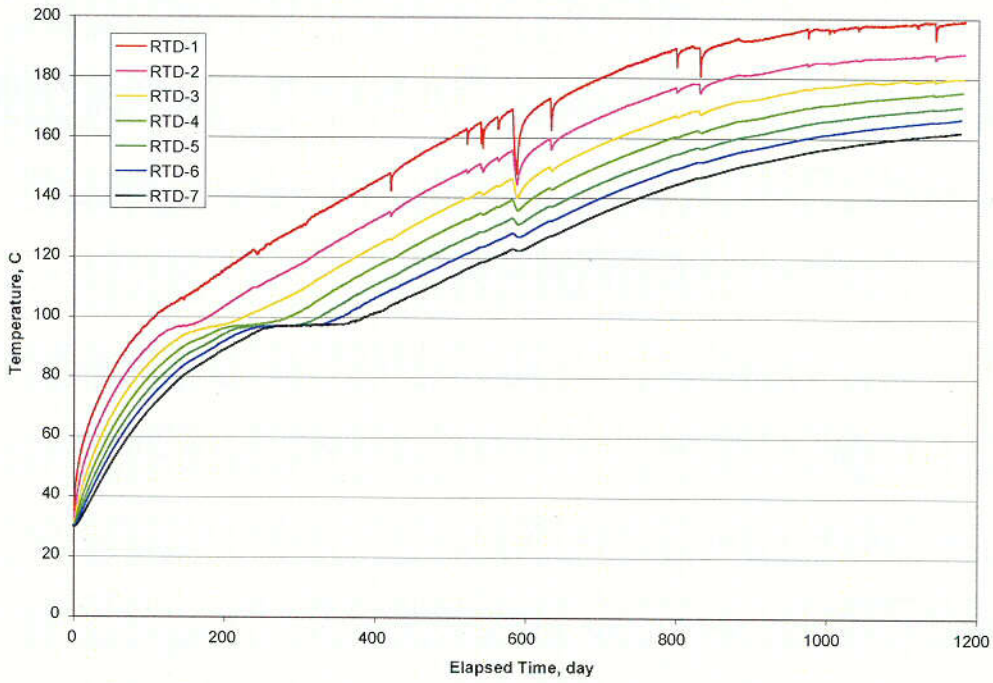


Figure 56. The temperature-time curves in borehole #175 show rapid evaporation process starts at RTD-5.

Temperature in hole#175, at 39m from the blukhead, 45 degree from AOD.

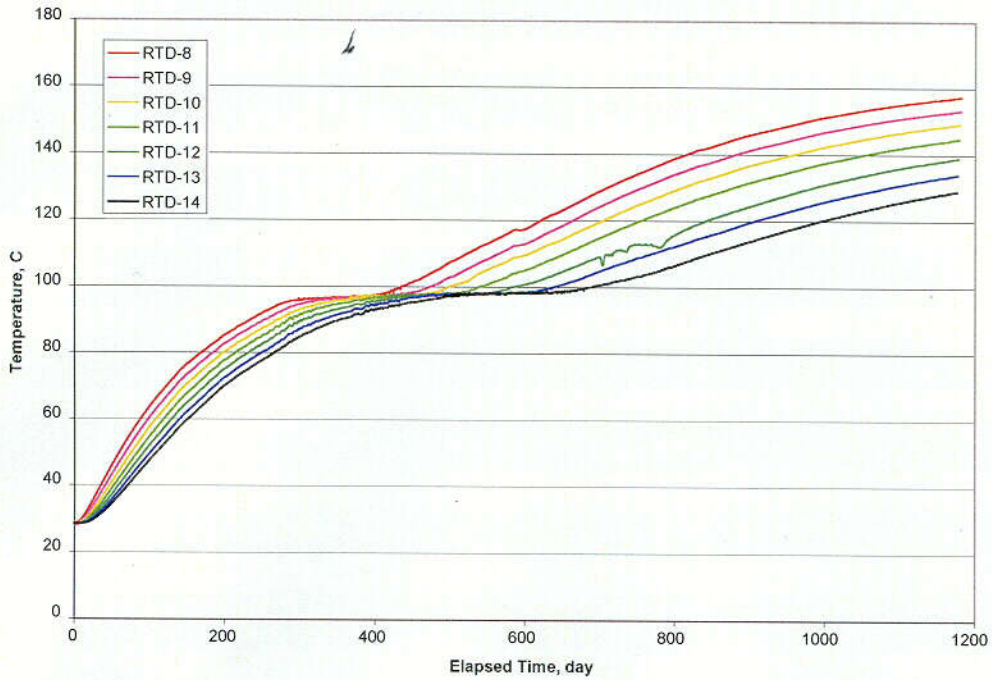


Figure 57. The temperatures in borehole #175 at RTD-8 to RTD-14 show flat regions indicating rapid evaporation.

Temperature in hole#175, at 39m from the bulkhead, 45 degree from AOD.

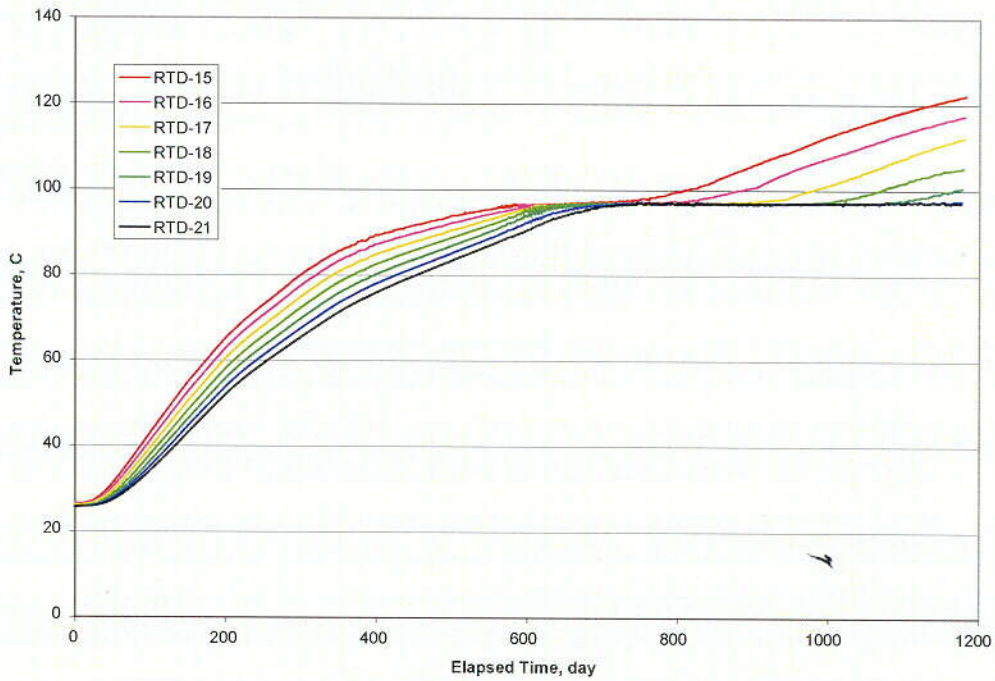


Figure 58. The temperature-time curves in borehole #175 show that the rapid evaporation process involves RTD-15 to RTD-21.

Temperature in hole#175, at 39m from the bulkhead, 45 degree from AOD.

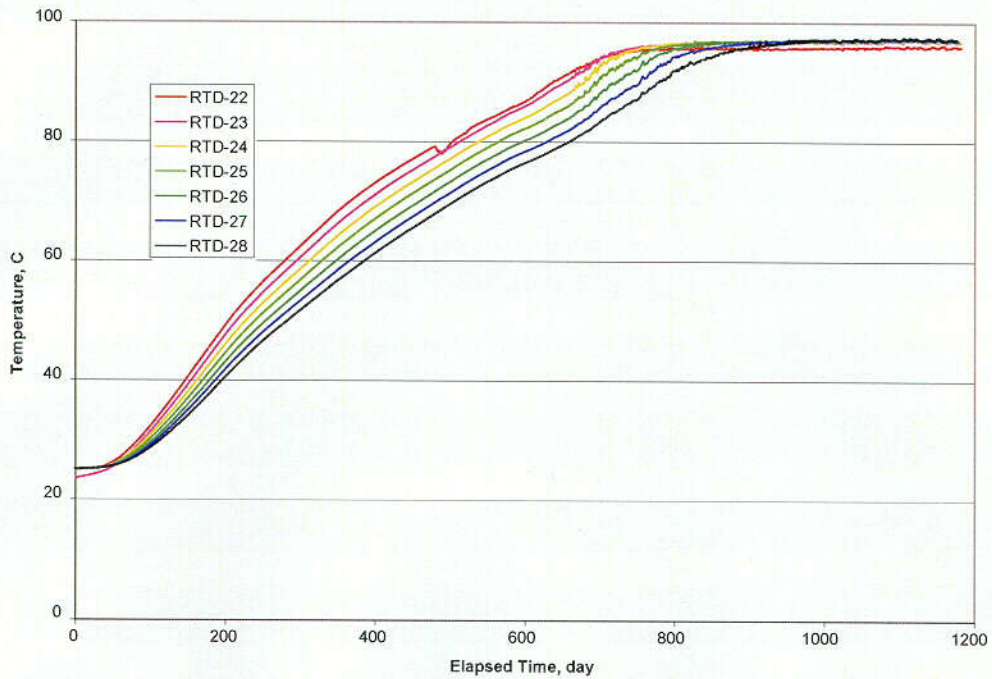


Figure 59. The temperature-time curves in borehole #175 show well-defined flat regions at RTD-22 to RTD-28.

Temperature in hole#172, at 39m from the bulkhead, -45 degree to AOD.

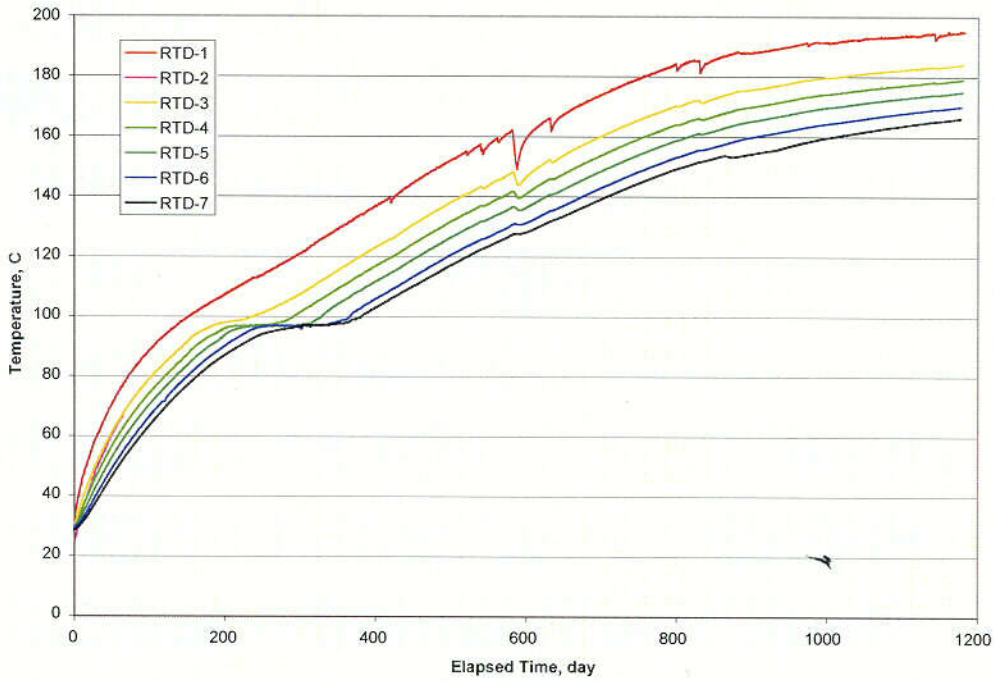


Figure 60. The temperature-time curves in borehole #172 show that the rapid evaporation process starts at RTD-4.

Temperature in hole#172, at 39m from the bulkhead, -45 degree to AOD.

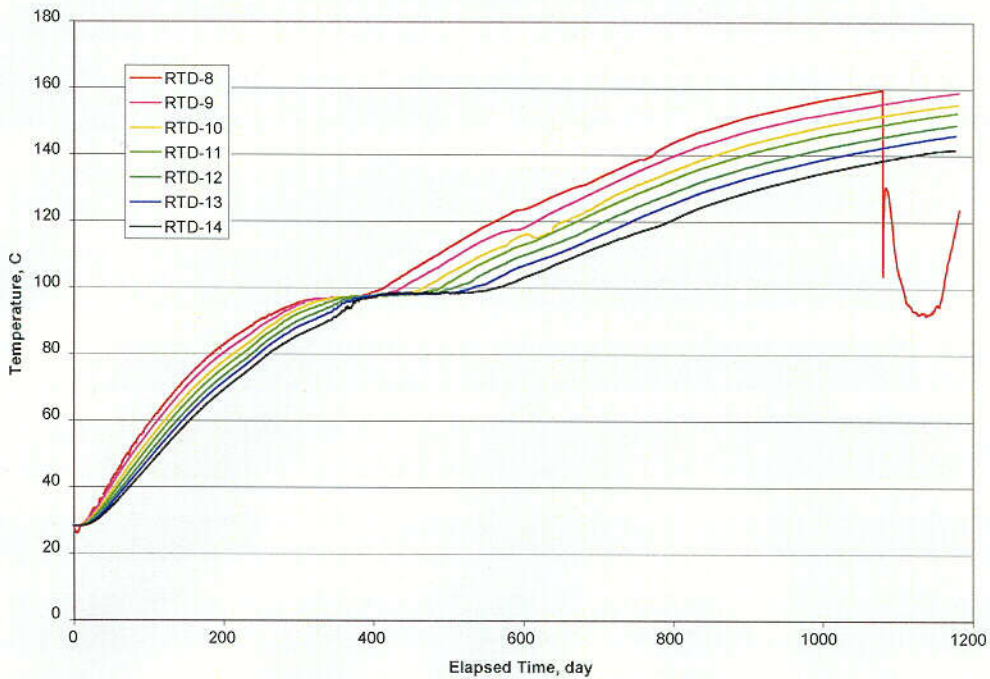


Figure 61. The temperature-time curves show that the rapid evaporation process involves all RTDs, RTD-8 to RTD-14, shown in here.

Temperature in hole#172, at 39m from the bulkhead, -45 degree to AOD.

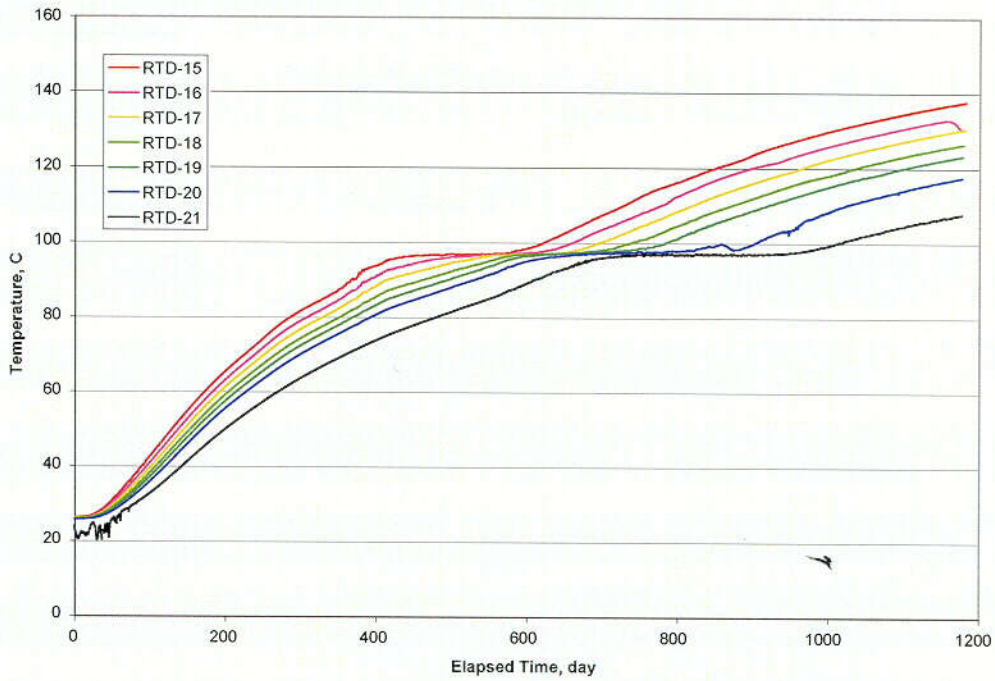


Figure 62. The temperature-time curves in borehole #172 show that RTD-15 to RTD-21 are involved in the rapid evaporation process.

Temperature in hole#172, at 39m from the bulkhead, -45 degree to AOD.

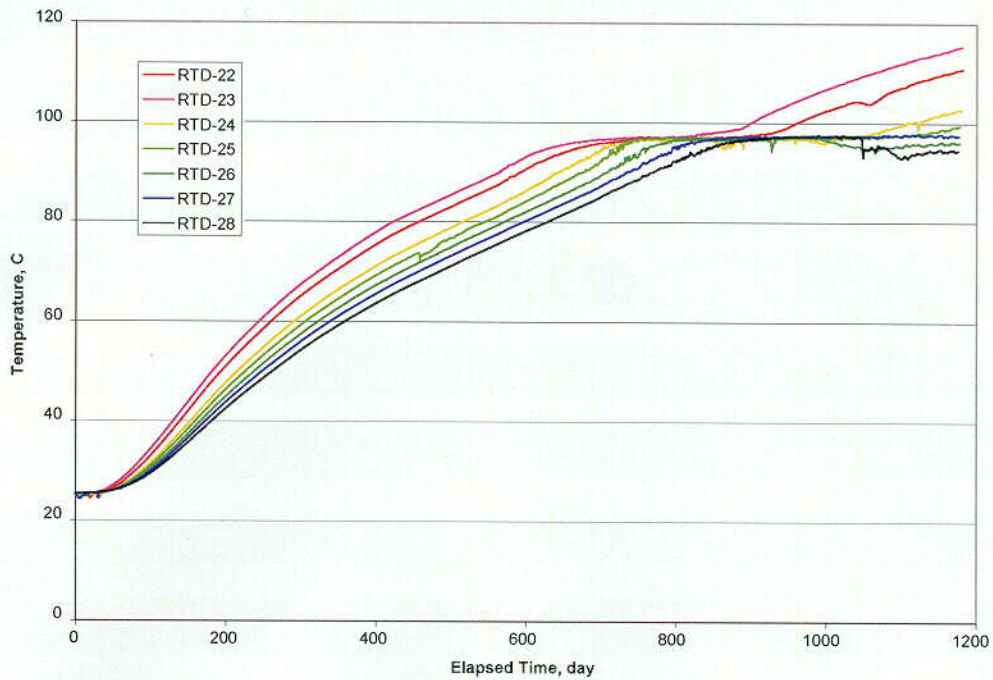


Figure 63. The temperature-time curves in borehole #172 at RTD-22 to RTD-28 show the effect of the rapid evaporation process.

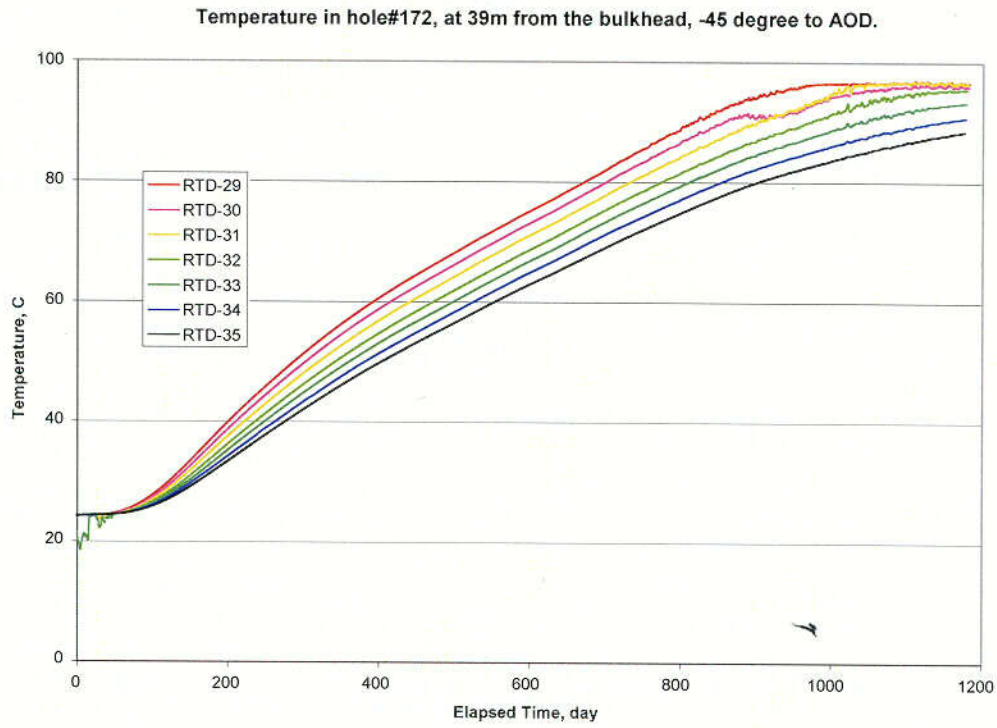


Figure 64. The temperature-time curves in borehole #172 show that at least RTD-29 to RTD-31 are involved in the rapid evaporation process.

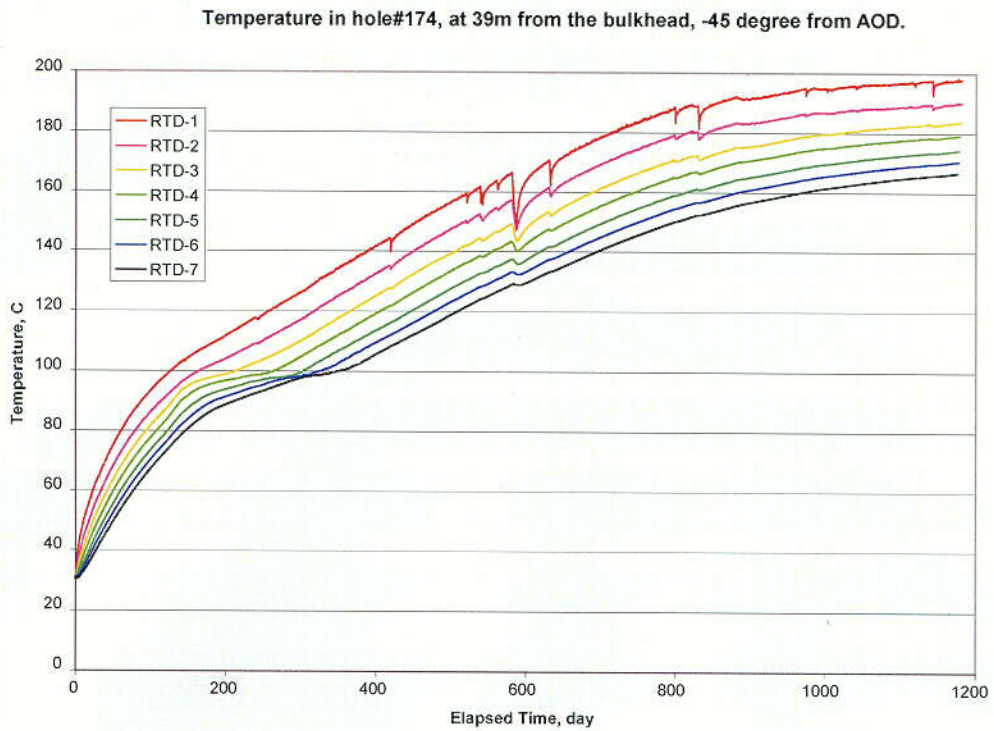


Figure 65. The temperature-time curve at RTD-7 in borehole #174 starts to show the effect of rapid evaporation.

Temperature in hole#174, at 39m from the bulkhead, -45 degree from AOD.

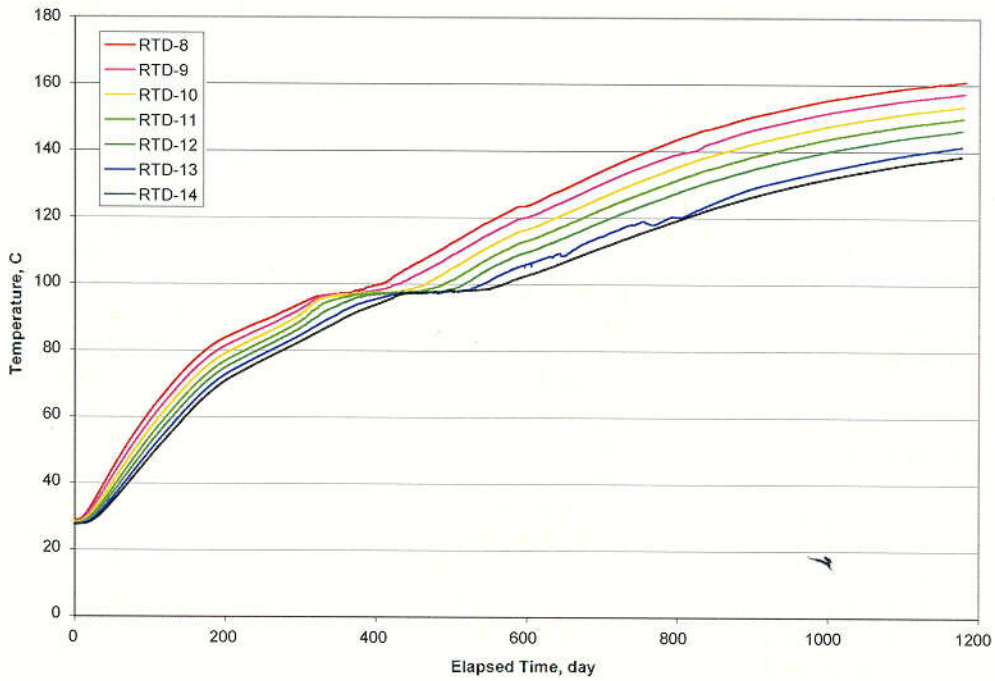


Figure 66. The temperature-time curves in borehole #174 at RTD-8 to RTD-14 show the effect of rapid evaporation.

Temperature in hole#174, at 39m from the bulkhead, -45 degree from AOD.

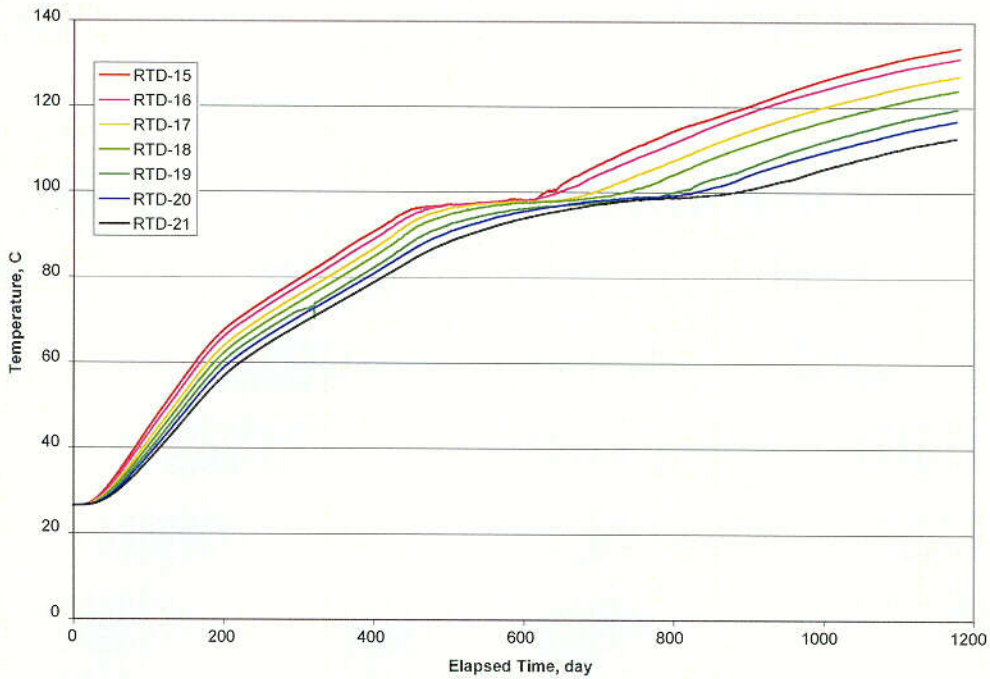


Figure 67. The temperature-time curves in borehole #174 at RTD-15 and RTD-16 show the effect of rapid evaporation.

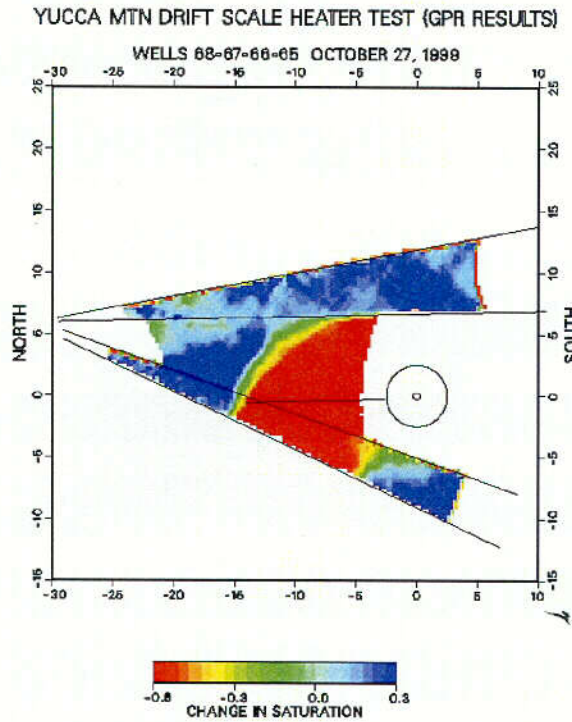


Figure 68. GPR results in boreholes #65 to #68. This figure shows the difference between the October 27, 1999 measurements and the pre-heat baseline on October 29, 1997.

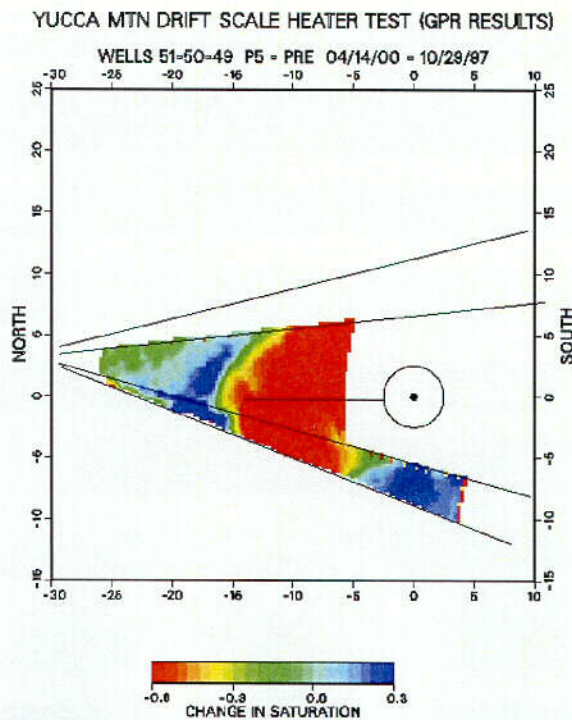


Figure 69. The GPR results in boreholes #49 to #51. This figure shows the difference between the measurements on April 14, 2000 and the pre-heat baseline on October 29, 1997.

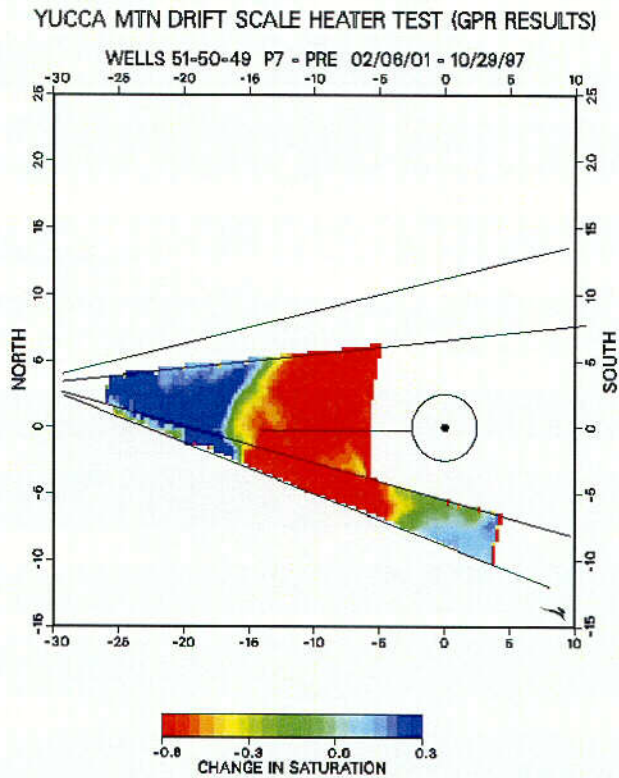


Figure 70. The GPR results in boreholes #49 to #51. This figure shows the difference between the measurements on February 6, 2001 and the pre-heat baseline on October 29, 1997.

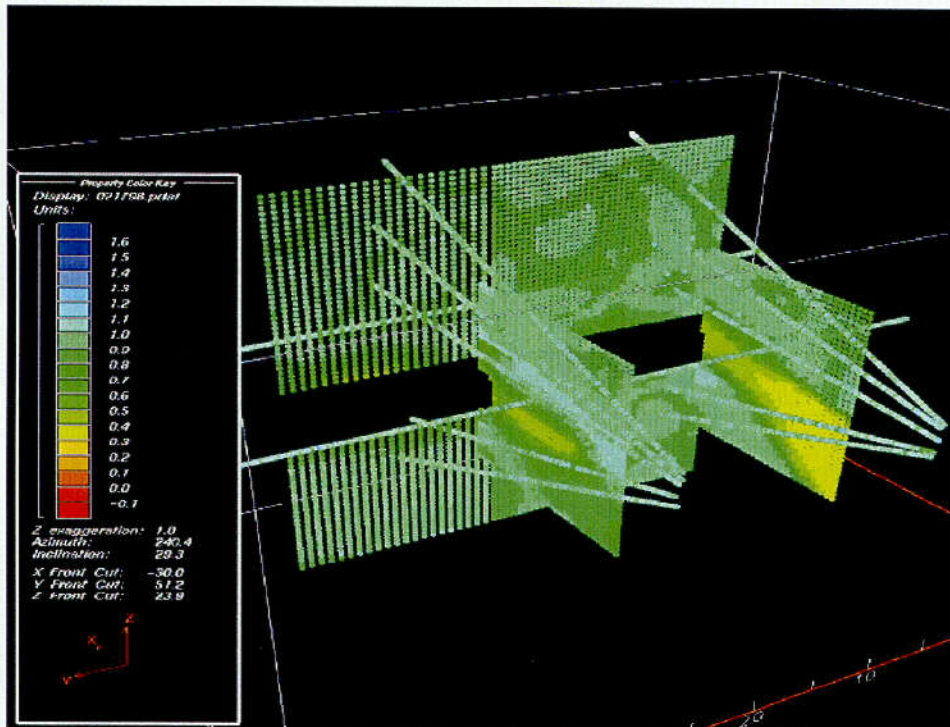


Figure 71. The ERT and neutron results in the DST. This figure shows the ratio of the water content measurements on 2/17/98 to that of the pre-heat baselines.

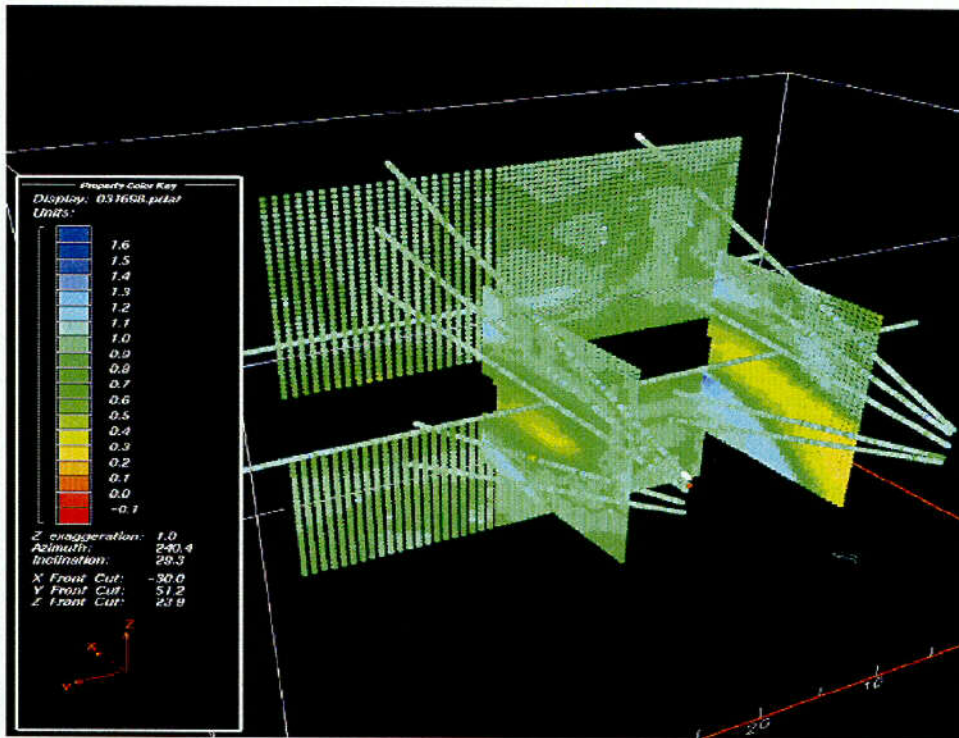


Figure 72. The ERT and neutron results in the DST. This figure shows the ratio of the water content measurements on 3/16/98 to that of the pre-heat baselines.

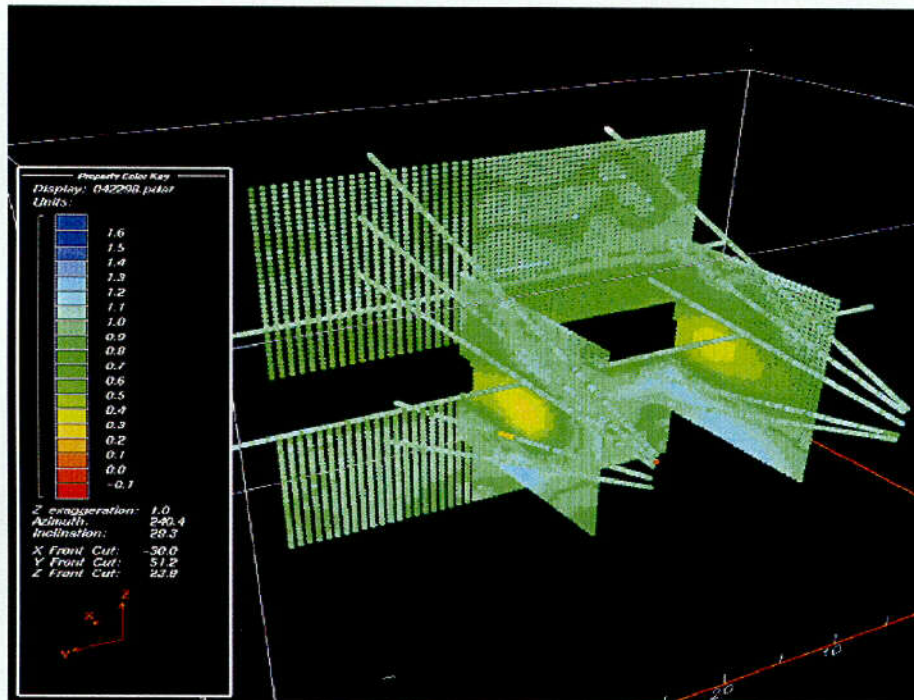


Figure 73. The ERT and neutron results in the DST. This figure shows the ratio between the water content measurements on 4/22/98 to that of the pre-heat baselines.

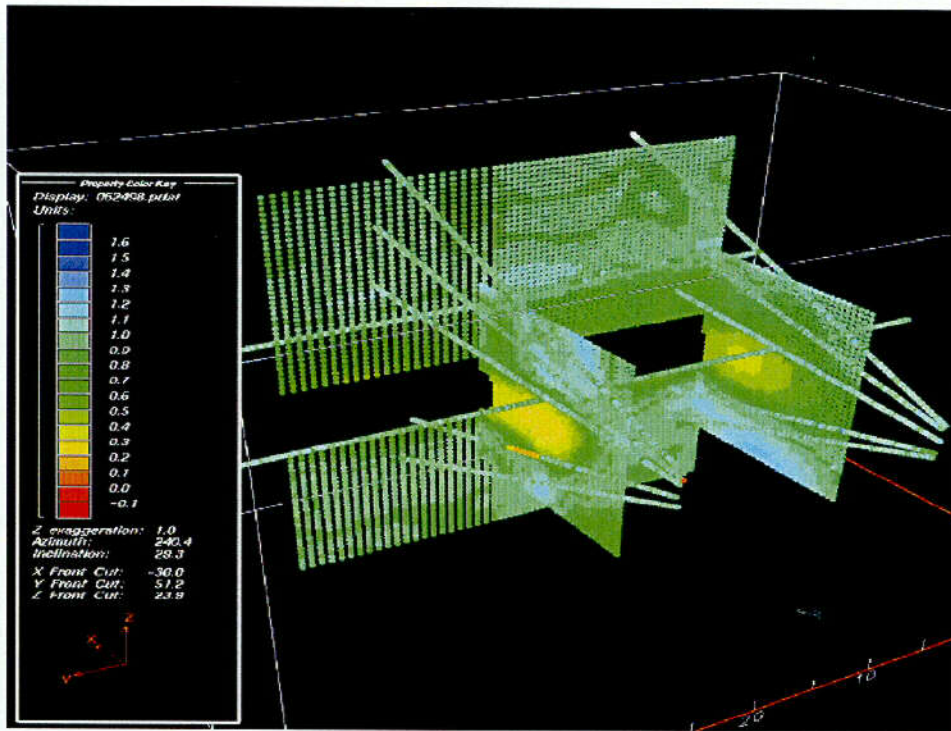


Figure 74. The ERT and neutron results in the DST. This figure shows the ratio between the water content measurements on 6/24/98 to that of the pre-heat baselines.

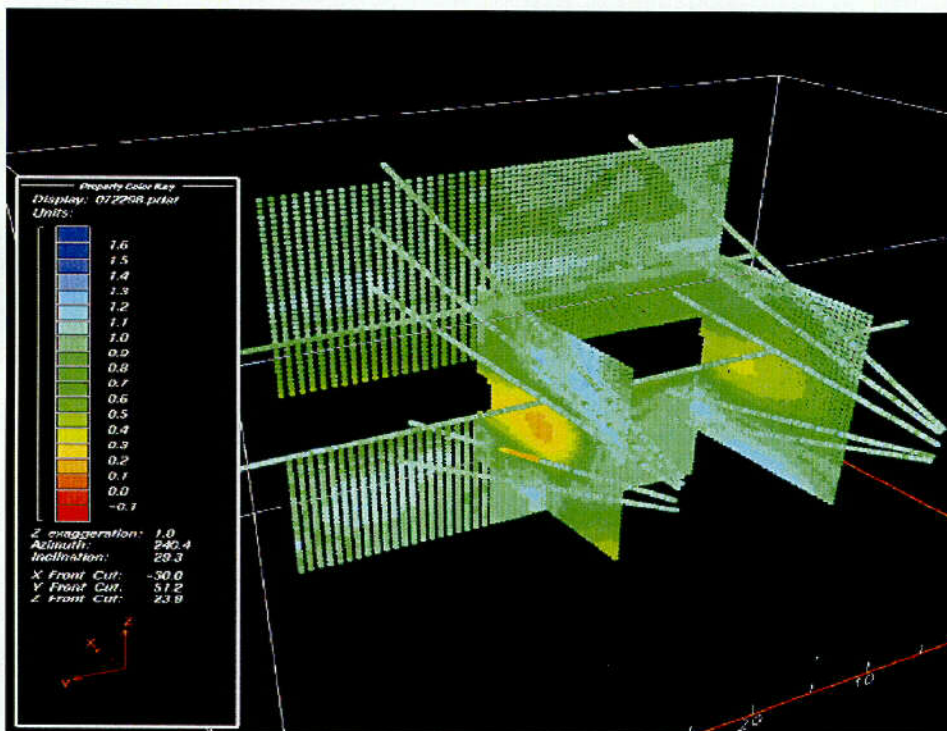


Figure 75. The ERT and neutron results in the DST. This figure shows the ratio between the water content measurements on 7/22/98 to that of the pre-heat baselines.

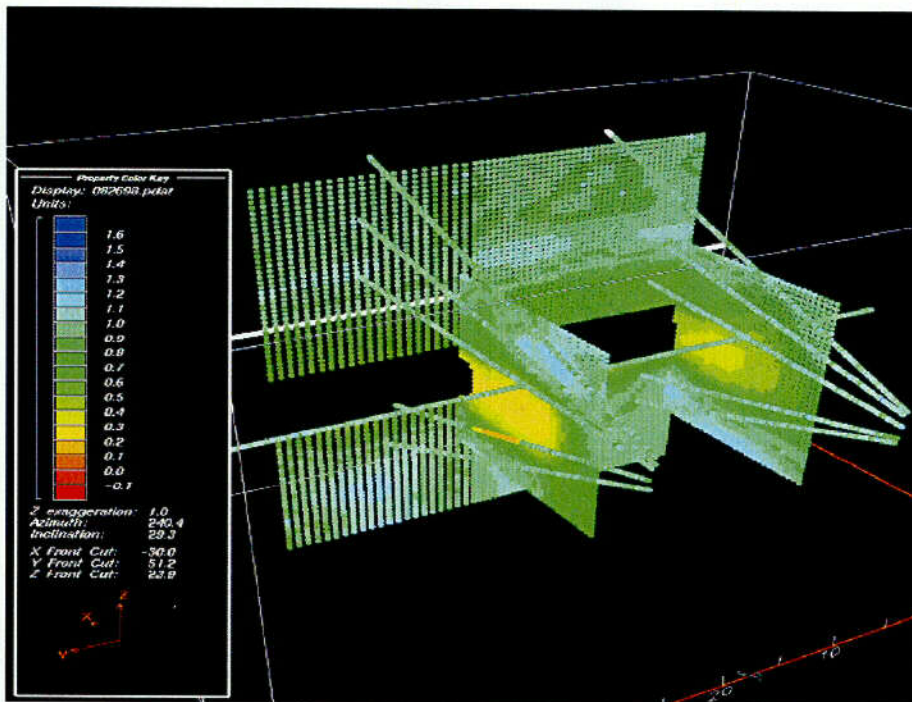


Figure 76. The ERT and neutron results in the DST. This figure shows the ratio between the water content measurements on 8/26/98 to that of the pre-heat baselines.

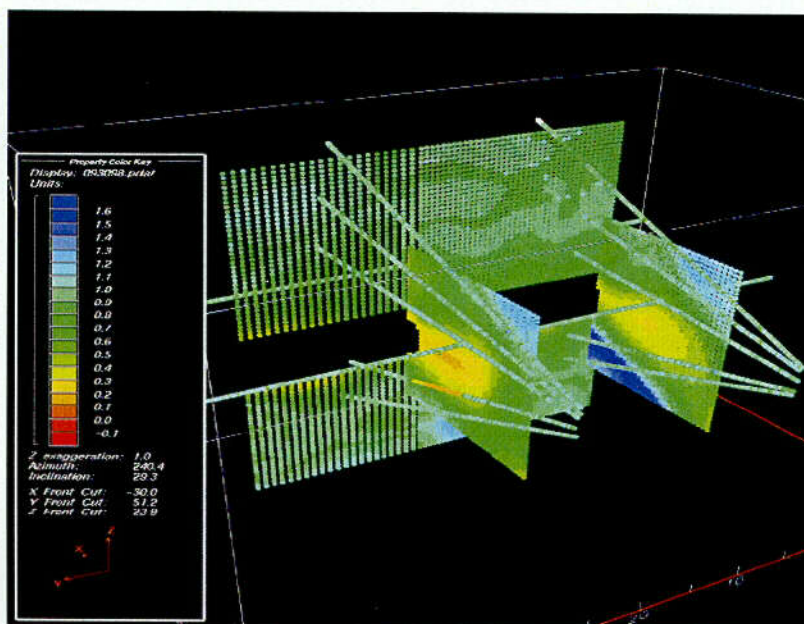


Figure 77. The ERT and neutron results in the DST. This figure shows the ratio between the water content measurements on 9/30/98 to that of the pre-heat baselines.

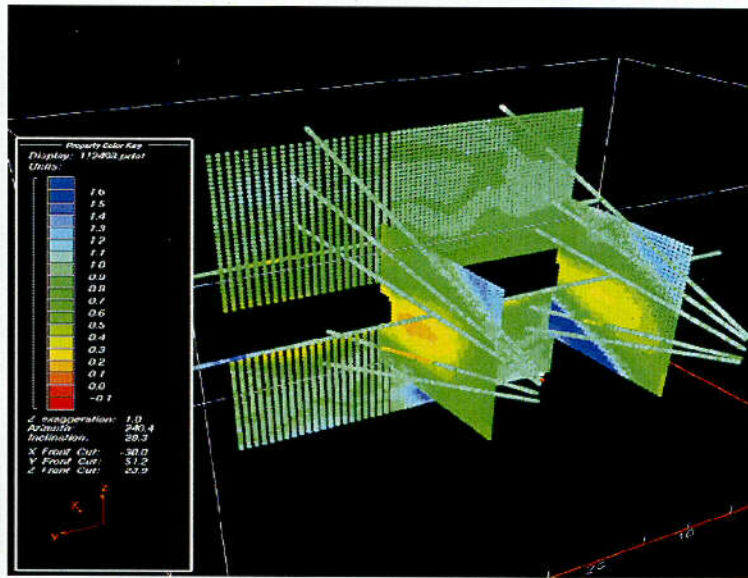


Figure 78. The ERT and neutron results in the DST. This figure shows the ratio between the water content measurements on 11/24/98 to that of the pre-heat baselines.

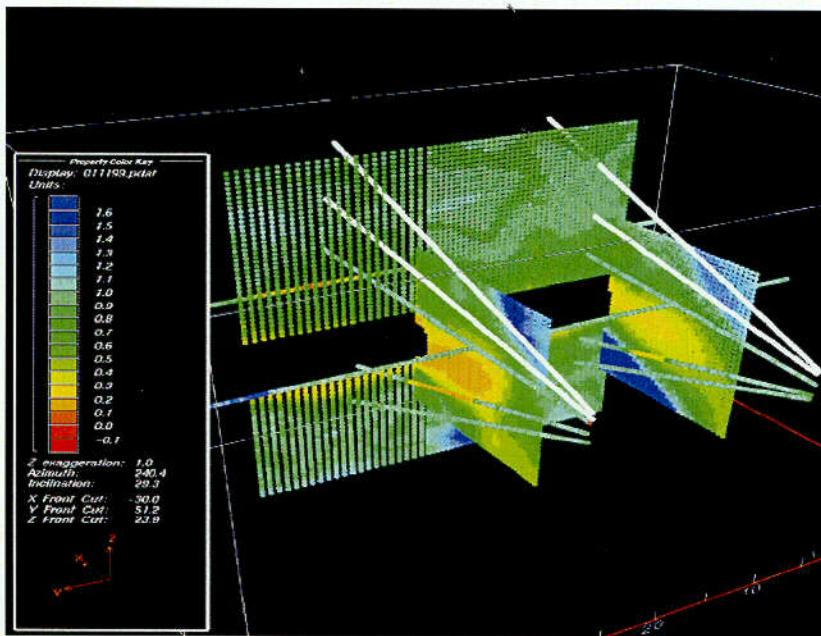


Figure 79. The ERT and neutron results in the DST. This figure shows the ratio between the water content measurements on 1/11/99 to that of the pre-heat baselines.

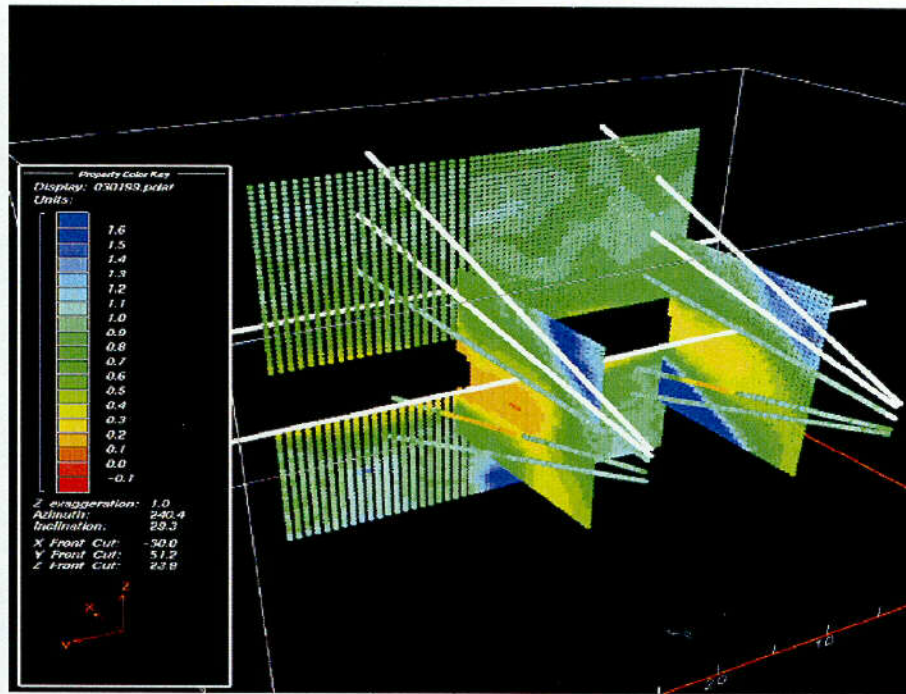


Figure 80. The ERT and neutron results in the DST. This figure shows the ratio between the water content measurements on 3/01/99 to that of the pre-heat baselines.

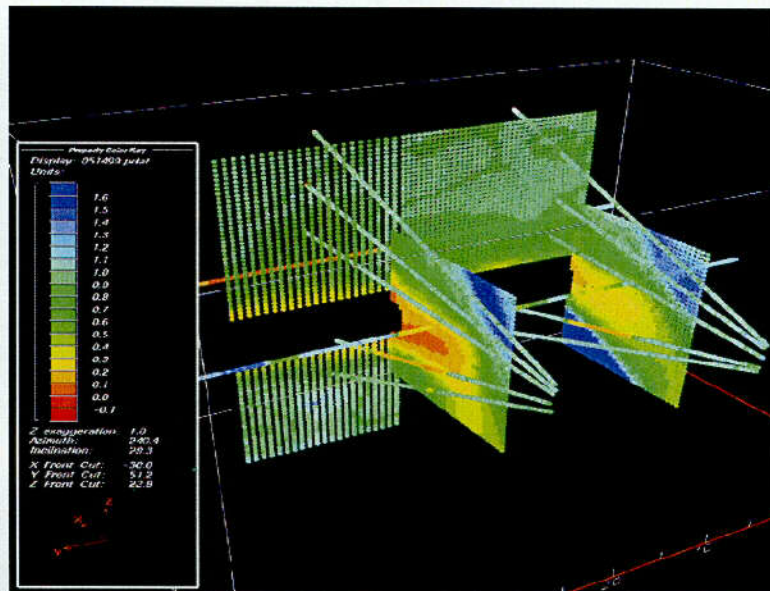


Figure 81. The ERT and neutron results in the DST. This figure shows the ratio between the water content measurements on 5/14/99 to that of the pre-heat baselines.

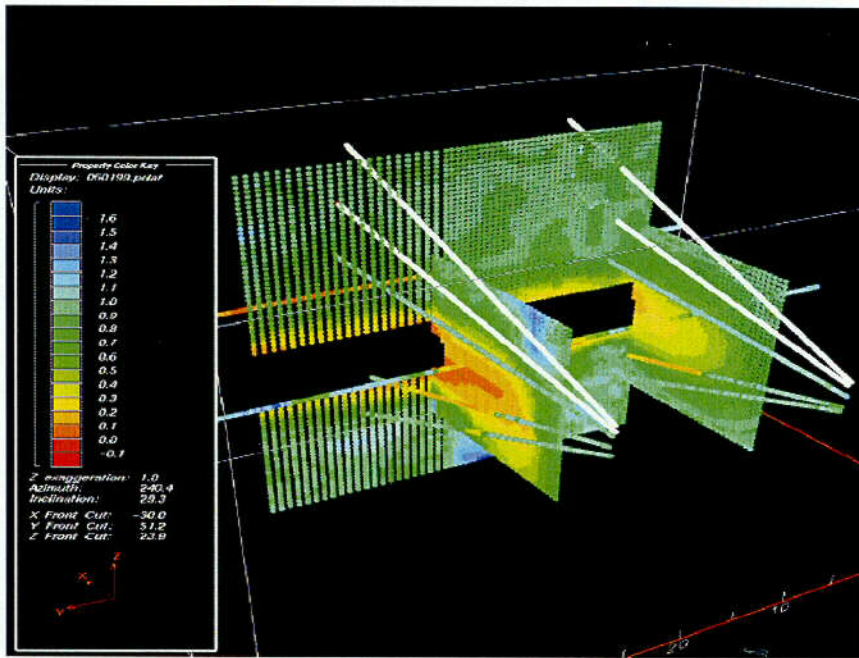


Figure 82. The ERT and neutron results in the DST. This figure shows the ratio between the water content measurements on 6/01/99 to that of the pre-heat baselines.

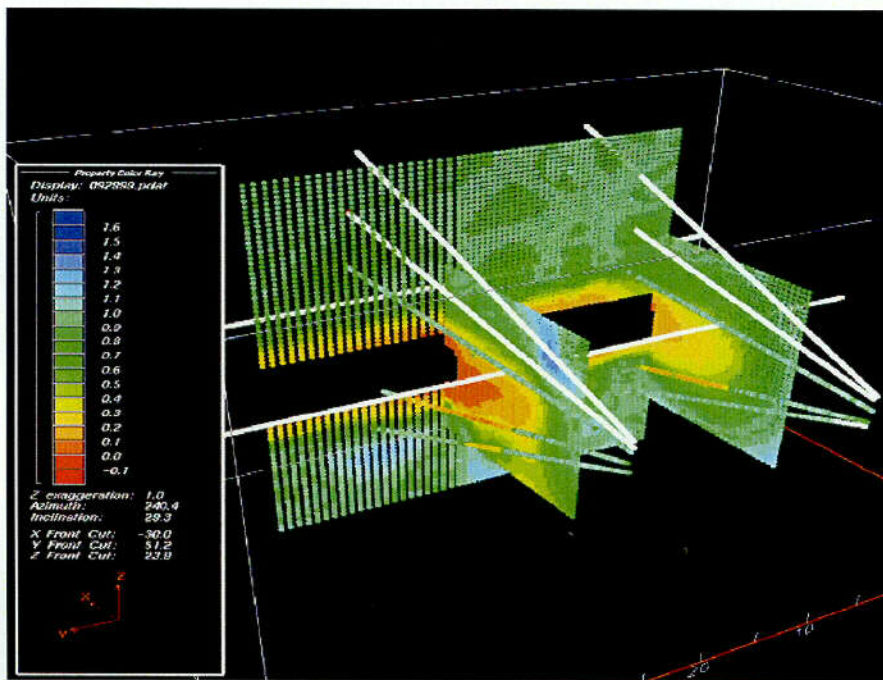


Figure 83. The ERT and neutron results in the DST. This figure shows the ratio between the water content measurements on 9/29/99 to that of the pre-heat baselines.

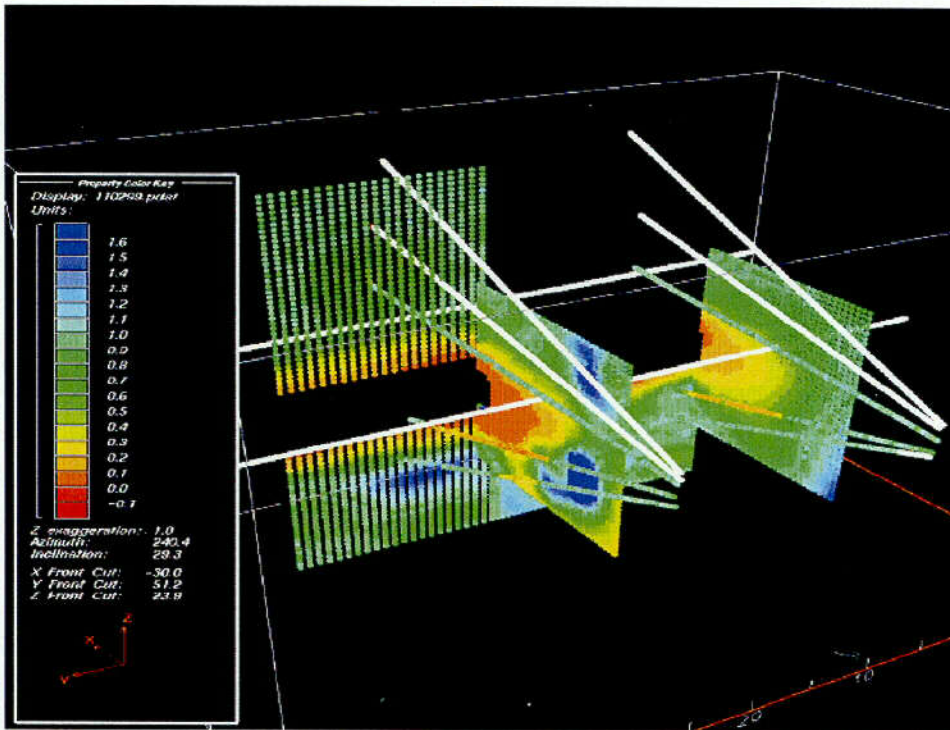


Figure 84. The ERT and neutron results in the DST. This figure shows the ratio between the water content measurements on 11/07/99 to that of the pre-heat baselines.

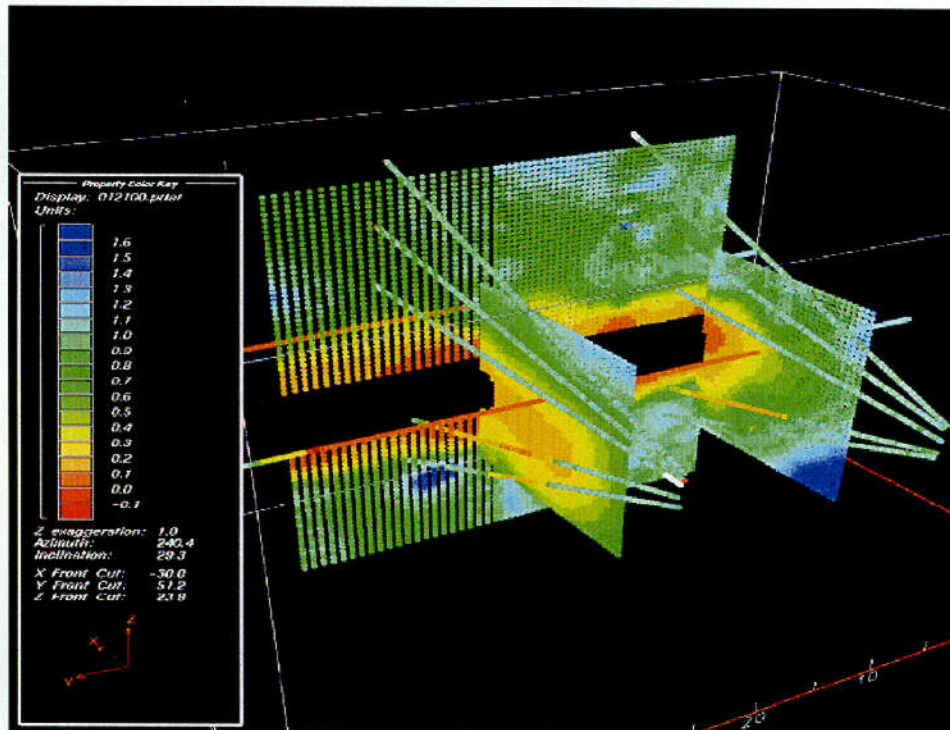


Figure 85. The ERT and neutron results in the DST. This figure shows the ratio between the water content measurements on 1/21/00 to that of the pre-heat baselines.

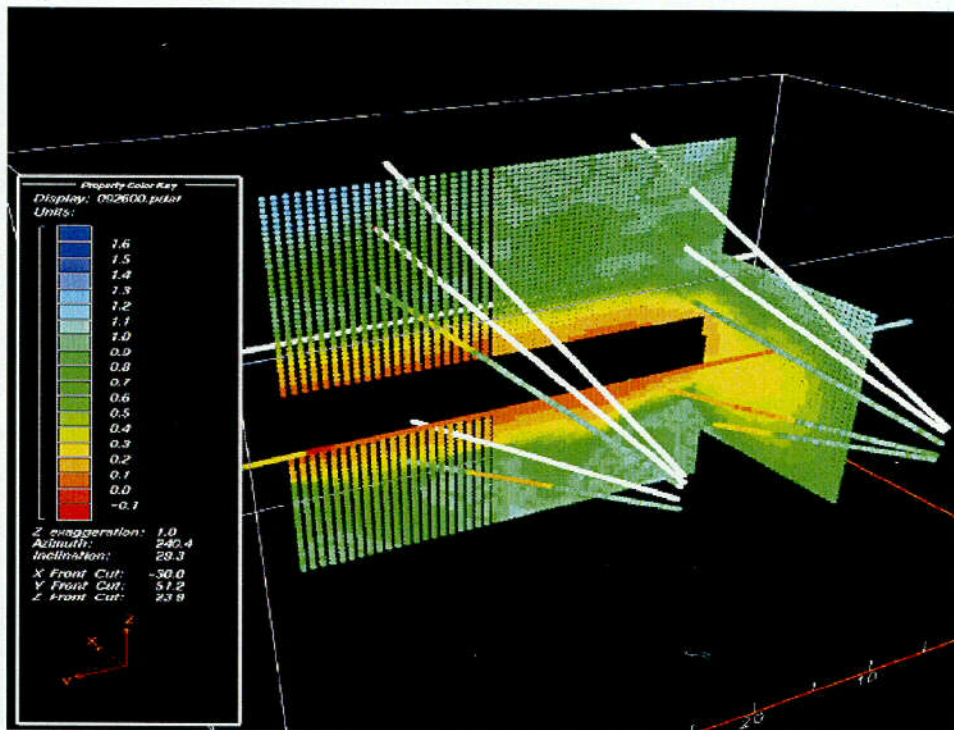


Figure 86. The ERT and neutron results in the DST. This figure shows the ratio between the water content measurements on 9/26/00 to that of the pre-heat baselines.

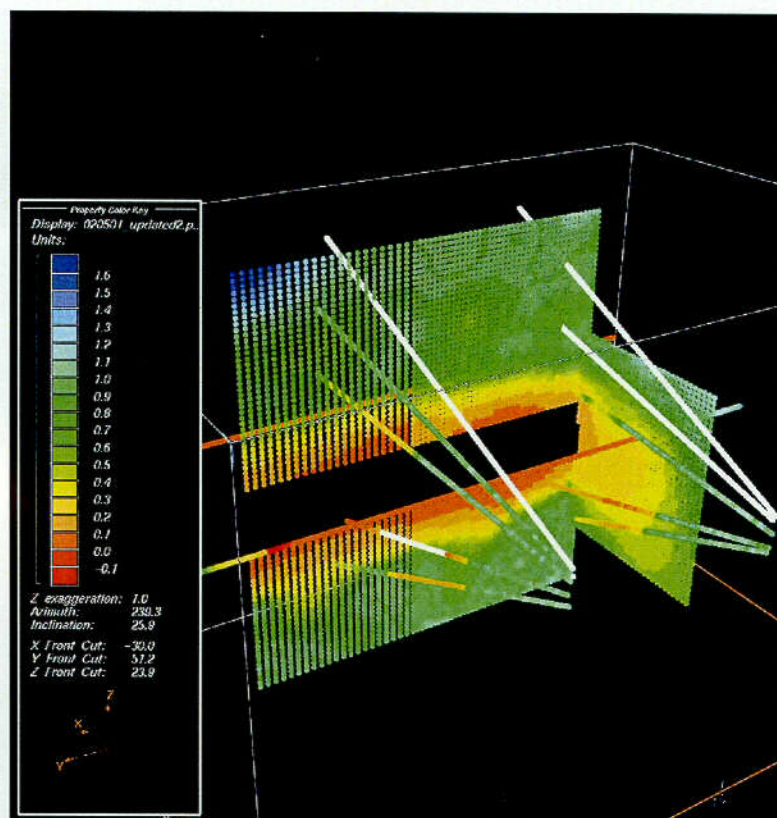


Figure 87. The ERT and neutron results in the DST. This figure shows the ratio between the water content measurements on 2/5/01 to that of the pre-heat baselines.